

Contents lists available at ScienceDirect

Energy

journal homepage: www.elsevier.com/locate/energy





Turbulence model effects on the hydrodynamic response of an oscillating water column (OWC) with use of a computational fluid dynamics model

Yuxin Zeng ^a, Wei Shi ^{a,b,*}, Constantine Michailides ^c, Zhengru Ren ^d, Xin Li ^b

- ^a DeepWater Engineering Research Centre, Dalian University of Technology, China
- ^b State Key Laboratory of Coastal and Offshore Engineering, Dalian University of Technology, Dalian, China
- ^c Civil Engineering, International Hellenic University, Greece
- ^d Institute for Ocean Engineering, Shenzhen International Graduate School, Tsinghua University, China

ARTICLE INFO

Keywords: Computational fluid dynamics Oscillating water columns Hydrodynamic performance Turbulence models Pressure distribution

ABSTRACT

Oscillating water column (OWC) is considered as one of the promising wave energy converters (WECs) due to its simple structure and working mechanism. Integrating OWCs with other marine structures gives additional feasible applications for WEC devices. This study presents a numerical simulation of a circular bottom-sitting OWC device for wave energy extraction using computational fluid dynamics. The numerical model is based on Reynolds Averaged Navier-Stokes equations with different turbulence models and a volume-of-fluid method to track the free surface. The numerical model and setup are validated against a set of wave-flume experimental results. The numerical simulation provides detailed flow-field information, which allows for an analysis of the spatial non-uniformity inside and outside of the OWC chamber. The results show that the SST $k-\omega$ turbulence model is recommended in OWC simulation, of this type, comparing the wave elevation and air pressure to experimental data. Moreover, positive results of the integration of an OWC of this type on a breakwater are presented and discussed.

1. Introduction

In recent years, the release of greenhouse gases caused by the massive exploitation of fossil energy has promoted the development of different types of marine renewable energy technologies [1]. According to statistics [2], the annual energy transferred from wind to the ocean is approximately $0.17~{\rm W/m^2}$. Additionally, the wave energy transferred from waves to global coastlines is approximately 32,000 TWh/yr [3]. Different types of marine renewable energy systems have been studied so far [4–6]. The average global wave energy resource contour over the past 30 years is presented in Fig. 1. Through the conversion of marine wave energy, energy requirements in both surrounding isolated islands and coastal cities will be effectively reduced [8].

Among all the kinds of wave energy extraction methods at sea, oscillating water column (OWC) is becoming the object of extensive research due to its simple working principle compared to other wave energy converter (WEC) technologies [9]. The general working principle of an OWC device is that a wave passes through the OWC chamber and causes a change in the wave surface and air within the chamber. This, in turn, drives air out of the chamber and specifically through a turbine to

generate electricity [10].

The operating mechanism of an OWC device is simple. As long as water level changes on sea surface, the conversion of mechanical energy to electrical energy can be realized. Among many systems that extract energy from ocean waves, the OWC concept is unique because it is the only technology that its key parts are natural components of the structure [9]. OWCs are composed of two key components, i.e., a collection chamber and a power take-off (PTO) system. The collection chamber generates aerodynamic force through the rise and fall of waves, and the PTO system converts aerodynamic power into electricity or other useable forms.

Many studies have been performed to examine the mechanism and dynamic performance of OWC devices. Zheng et al. [11] studied the integration of an OWC into a vertical tubular structure. They found that a thinner wall thickness of the chamber was beneficial to the produced power. Hashem et al. [12] analyzed an innovative OWC device that uses water instead of air as the working fluid. The results show that the torque of the hydraulic turbine is approximately 1.4 times larger than that of the traditional air turbine, and the torque coefficient is greatly improved. The results from Ning et al. [13] and Haghighi et al. [14]

^{*} Corresponding author. DeepWater Engineering Research Centre, Dalian University of Technology, China. E-mail address: weishi@dlut.edu.cn (W. Shi).

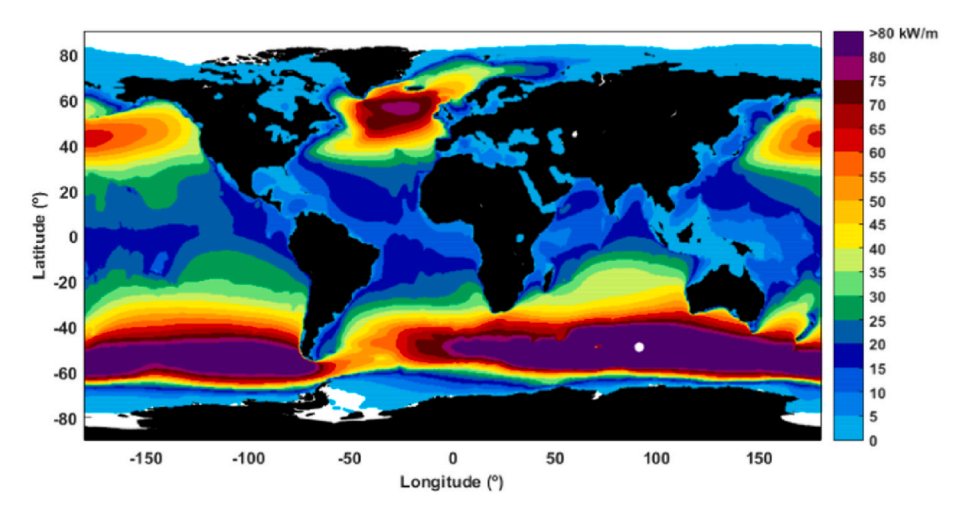


Fig. 1. Mean wave power over a 30-year time interval (1989–2018) [7].

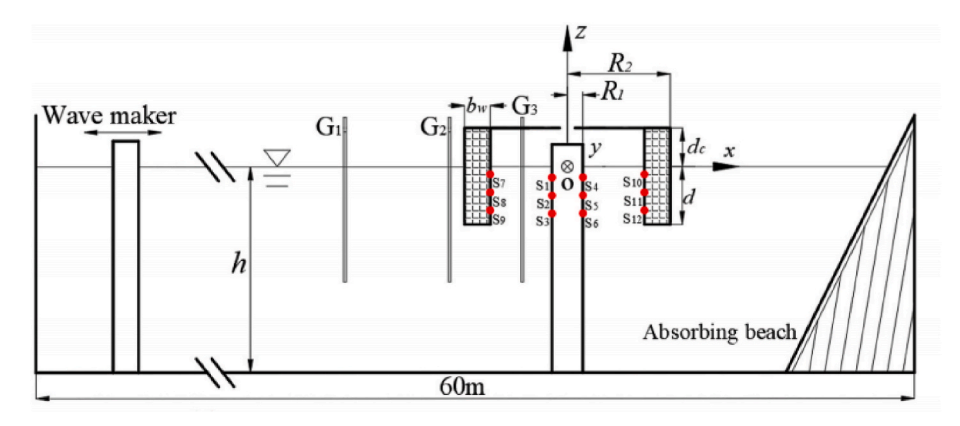


Fig. 2. Experimental layout: a side view showing the OWC device, the wave gauges and the pressure sensors [29].

Table 1 Positions of the pressure sensors.

	Position (m)		Position (m)		Position(m)		Position(m)
S_1	(-0.1,0,-	S_4	(0.1,0,-	S_7	(-0.3,0,-	S_{10}	(0.3,0,-
	0.1)		0.1)		0.07)		0.07)
S_2	(-0.1,0,-	S_5	(0.1,0,-	S_8	(-0.3,0,-	S_{11}	(0.3,0,-
	0.2)		0.2)		0.17)		0.07)
S_3	(-0.1,0,-	S_6	(0.1,0,-	S_9	(-0.3,0,-	S_{12}	(0.3,0,-
	0.3)		0.3)		0.27)		0.07)

show that the dual-chamber OWC device has a good effect in improving the peak efficiency and effective bandwidth compared to the single-chamber OWC device, and has two resonance frequencies. Although many scholars have made significant contributions to the hydrodynamic performance of OWC devices, such as McCormick [15] and Evans [16], most of the numerical models are based on linear wave assumption and ignore viscosity, failing to achieve accurate predictions.

With the rapid development of computational power, computational fluid dynamics (CFD) has become a feasible tool to study complex fluid-structure coupling effects [17]. Compared to expensive experimental campaigns, the advantages of the CFD technique is the affordable numerical simulations and data accessibility at any point in the flow field. OWC devices have been analyzed using CFD methods in recent years [18–26]. Numerical results of Xu et al. [18] show that vortex shedding at the sharp edge of the OWC chamber enhances the spatial non-uniformity inside the OWC chamber through a resonant sloshing mechanism. Mohammad et al. [19] established a fixed multi–chamber OWC model.

The research indicates that the increase of incident wave height will result to the reduction of the device capture width ratio, but a noticeable improvement is presented for long wave periods. Dai et al. [20] used the CFD method to study the performance of OWC at different model scales. The Reynolds number effect in the study mainly introduces the hydrodynamic scale effect. The results show that the comparison between the different tank test results and the CFD simulation results shows that the CFD simulation can reproduce the hydrodynamic scale effects well. Cui et al. [21] bridge the knowledge gap between engineering applications and CFD achievements for this type of turbine. Recent developments in CFD modeling, geometry optimization and performance enhancements are summarized. Views on CFD models of axial turbines and their future trends are also presented. Based on the findings in literature review the use of different turbulence models is a very important factor in CFD calculations for OWCs. Liu et al. [27] studied the results of different SST $k - \omega$ turbulence models for wave-breaking conditions. By comparing the breaking point, free surface elevation and time-averaged turbulent kinetic energy, it is found that the SST $k - \omega$ model is the most accurate in comparing experimental data and capturing physical phenomena. Under coastal conditions, the $k - \varepsilon$ turbulence model is also widely used to study the interaction between waves and underwater structures. Wu et al. [28] used the $k-\varepsilon$ turbulence model to simulate the propagation of solitary waves across two isolated underwater structures. The results show that under specified wave conditions, the optimal horizontal distance between two underwater structures is 2.5 times the depth of still water. The results of CFD simulations can be greatly affected by the selection of a different turbulence model.

The cost-sharing strategy of combining or integrating two or more

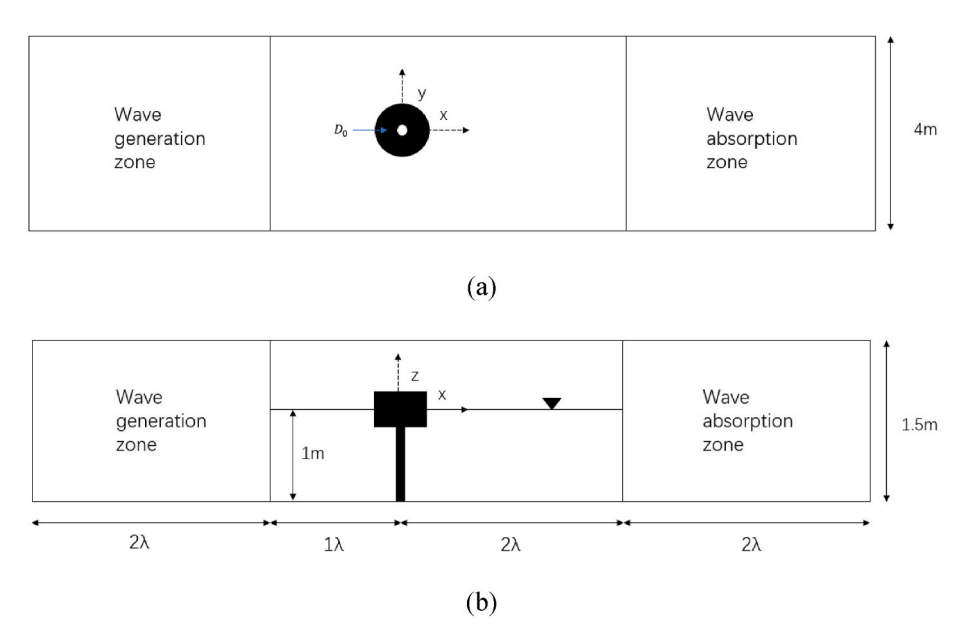


Fig. 3. Sketch of the numerical wave tank: (a) Top view; (b) Front view.

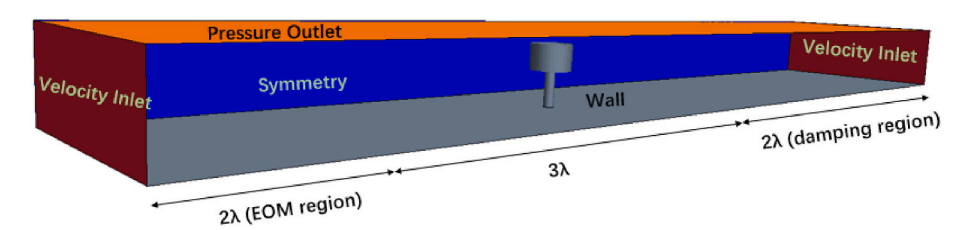


Fig. 4. Numerical wave tank model.

Table 2
Transport equations of three turbulence models.

turbulence model	transport equations
Standard $k - \omega$	$\frac{\partial}{\partial t}(\rho k) + \frac{\partial}{\partial t}(\rho u_j k) = \tau_{ij}\frac{\partial u_i}{\partial x_j} - \beta^* \rho \omega k + \frac{\partial}{\partial x_j}[(\mu + \sigma^* \mu_T)]$
	$\begin{array}{lcl} \frac{\partial k}{\partial x_{j}} \\ \\ \frac{\partial}{\partial t}(\rho \omega) & + & \frac{\partial}{\partial x_{j}}(\rho u_{j}\omega) & = & (\gamma \omega/k)\tau_{ij}\frac{\partial u_{i}}{\partial x_{j}} - & \beta \rho \omega^{2} & + & \frac{\partial}{\partial x_{j}}[(\mu +)^{2} +)^{2} + & \frac{\partial}{\partial x_{j}}(\mu +)^{2} \\ \end{array}$
	$\sigma\mu_T)rac{\partial\omega}{\partial x_j}]$
SST $k - \omega$	$\frac{\partial}{\partial t}(\rho k) + \frac{\partial}{\partial t}(\rho u_j k) = \tau_{ij}\frac{\partial u_i}{\partial x_j} - \beta^* \rho \omega k + \frac{\partial}{\partial x_j}[(\mu + \sigma_k \mu_T)]$
	$\frac{\partial k}{\partial x_j}$]
	$\frac{\partial}{\partial t}(\rho\omega) + \frac{\partial}{\partial x_j}(\rho u_j\omega) = \frac{\gamma}{\mu_T} \tau_{ij} \frac{\partial u_i}{\partial x_j} - \beta\rho\omega^2 + \frac{\partial}{\partial x_j} [(\mu + \frac{\partial}{\partial x_j} - \frac{\partial}{\partial x_j} -$
	$\sigma_k \mu_T) rac{\partial \omega}{\partial x_j} \ + \ 2 ho (1 - F_1) \sigma_k^* rac{1}{\omega} rac{\partial k}{\partial x_j} rac{\partial \omega}{\partial x_j}$
Realizable $k-$	$\frac{\partial}{\partial t}(\rho k) + \frac{\partial}{\partial x_i}(\rho k u_i) = \frac{\partial}{\partial x_j}[(\mu + \frac{\mu_T}{\sigma_k}) \frac{\partial k}{\partial x_j}] + G_k + G_b -$
	$\begin{array}{lcl} \rho \varepsilon & -Y_M & +S_k \\ \frac{\partial}{\partial t}(\rho \varepsilon) & + & \frac{\partial}{\partial x_i}(\rho \varepsilon u_i) & = & \frac{\partial}{\partial x_j}[(\mu + \frac{\mu_T}{\sigma_\varepsilon}) \; \frac{\partial \varepsilon}{\partial x_j}] \; + \; \rho C_1 S \varepsilon \; \; - \end{array}$
	$ ho C_2 rac{arepsilon^2}{k + \sqrt{\mu_t arepsilon/ ho}} \;\; + \;\; C_1 rac{arepsilon}{k} C_{3arepsilon} G_b \;\; + \;\; S_arepsilon$

different marine structures into one installation is one of the solutions to reduce the construction cost of OWCs. Present research indicates that although the technical solutions of OWC utilization are mature to some extent, the high construction cost is one of the main obstacles restricting

the commercialization of OWC technology. Through integration, the space and cost-sharing of the combined structures can be achieved. Therefore, the cost per structure can be effectively reduced, resulting in more feasible engineering applications of wave energy devices in the future.

The possibility of integrating an OWC with fixed-breakwater is examined in this paper. To study the responses of an OWC, a numerical model is developed based on the CFD method in Section 3. The convergence of the grid size and the time step is examined. Different turbulence models, including standard $k-\omega$, SST $k-\omega$, and realizable $k-\varepsilon$, are compared against experimental data to verify the efficiency of the developed model and quantify the rationality of the selection of the turbulence model for the OWC examined here. The surface elevation of the model, pressure in the chamber of the OWC and pressure at specific points close to the supporting structure for the case of different kh numbers are presented and discussed. Research data shows that when different turbulence models are used, there will be a certain gap in the hydrodynamic efficiency obtained.

2. Experimental model

An experimental campaign using an 1:20 model was conducted in the wave-current flume at the State Key Laboratory of Coastal and Offshore Engineering in the Dalian University of Technology. The dimensions of the flume are 60 m long, 4 m wide and 2.5 m high. The layout of the experiment is shown in Fig. 2. The water depth is equal to 1 m. The radius of the support structure, R_1 , is 0.1 m and the radius of the OWC chamber, R_2 , is 0.4 m. The draft of the OWC chamber wall, d, is 0.3 m. The thickness of the chamber, b_w , is 0.1 m. Two pressure sensors positioned at the top of the chamber, i.e. S_{a1} (0.11 m, 0.11 m, 0.2 m) and

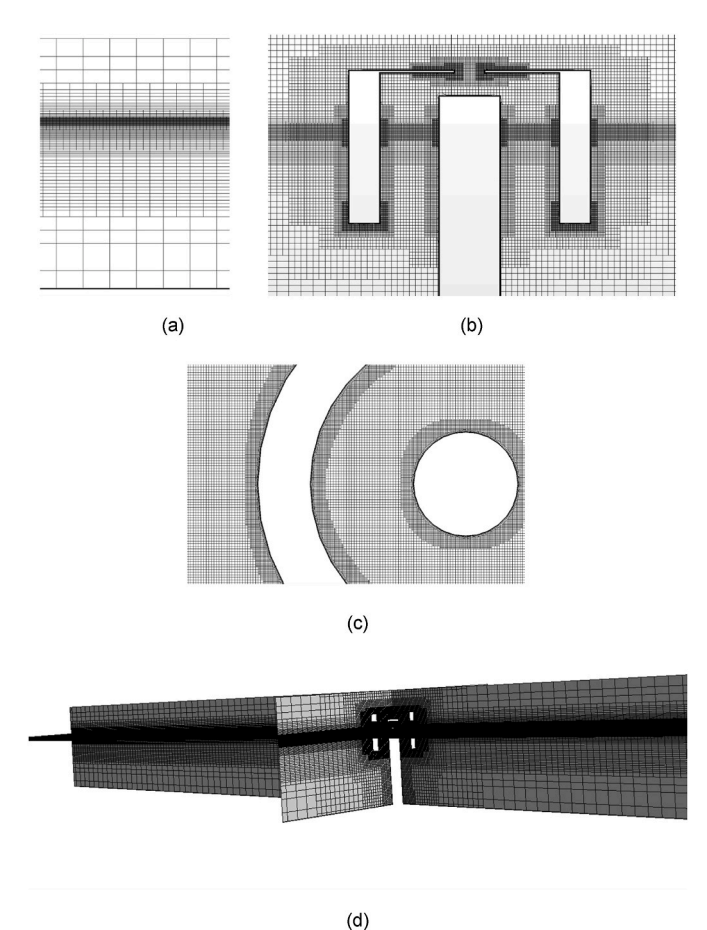


Fig. 5. 2D Meshing scheme of the numerical wave tank: (a) mesh distribution along water depth direction; (b) Mesh distribution around the structure (front view); (c) Mesh distribution around the structure (top view); (d) overview of mesh distribution.

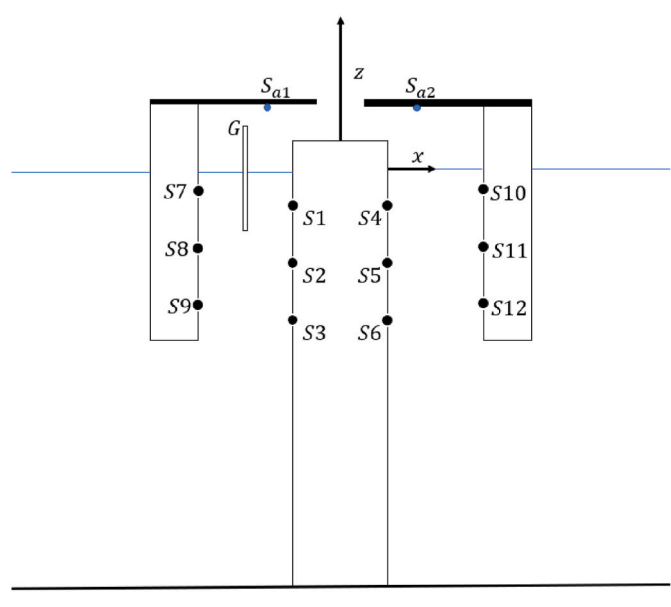


Fig. 6. Arrangement of measuring points.

 S_{a2} (-0.11 m, -0.11 m, 0.2 m), were used to record the air pressure, while, G_3 (-0.2 m, 0 m) was positioned to measure surface elevation. Twelve pressure sensors (S_1 $-S_{12}$) with positions presented in Table 1,

were placed around the OWT monopile and the OWC chamber wall (Fig. 2). The pneumatic damping induced by the PTO system in the experiment could be modeled by using an orifice or a slot to simulate an impulse turbine. In order to simulate the effects of nonlinear turbine damping, a circular orifice (0 m, 0 m, 0.2 m), with a diameter Do = 0.104 m was used in the this experimental campaign. The detailed experiment set up can be found in Ref. [29].

3. Numerical model

Relevant to the experiment, the layout of the numerical wave tank is given in Fig. 3. In the numerical wave tank, the direction of wave propagation is taken as the x-axis. The directions of the y-axis and z-axis are shown in the same figure, and the center of the model is placed at the intersection of the x-axis and the y-axis. The lengths of the wave generation zone and absorption zone are 2λ , respectively, where, λ is the wave length.

3.1. Flow field model

To simulate the air-water two phase interaction problem for the integrated structure, a three-dimensional numerical wave flume was built using the CFD tool STAR-CCM+ (Version: 2019.3.1). STAR-CCM+ utilizes the finite volume method and the integral formulation of the conservation equations for mass and momentum.

The continuity equation is given as:

$$\frac{\partial}{\partial t} \int_{V} \rho dV + \oint_{A} \rho \mathbf{v} \cdot ds = 0 \tag{1}$$

and the momentum equation is:

$$\frac{\partial}{\partial t} \int_{V} \rho \mathbf{v} dV + \oint_{A} \rho \mathbf{v} \mathbf{v}^{T} \cdot d\mathbf{s} = -\oint_{A} p \mathbf{I} \cdot d\mathbf{s} + \oint_{A} \mathbf{T} \cdot d\mathbf{s} + \int_{V} \mathbf{f}_{\mathbf{b}} dV + \int_{V} \mathbf{s}_{\mathbf{u}} dV$$
(2)

where ρ is the density of the fluid, V is a control volume, \mathbf{s} is the area vector and its direction is perpendicular to the area plane, $\mathbf{v}=(\mathbf{u},\mathbf{v},\mathbf{w})$ is the velocity field of fluid in Cartesian coordinates, p is the pressure acting on the area unit and \mathbf{T} is the viscous stress tensor, \mathbf{f}_b is the resultant volume force acting on the control volume, and \mathbf{s}_u is the source term specified by the user.

3.2. Free surface capturing

The volume-of-fluid (VOF) and high-resolution interface-capturing (HRIC) methods [30] are used to capture the free surface. In this simulation, the HRIC angle coefficient was set equal to 0.05. The VOF method uses the volume fraction of water in each grid to capture the liquid surface. The volume fraction α of the water phase is defined as

$$\alpha = \frac{V_w}{V} \tag{3}$$

where V_w is the volume of the water phase in the control volume. The value of α varies between 0 and 1. When α is equal to 0 there is no water in the control volume, while, when α is equal to 1 denotes that the control volume is filled with water.

The transport equation for α is [31].

$$\frac{\partial}{\partial t} \int_{V} \alpha dV + \oint_{A} \alpha \mathbf{v} \cdot d\mathbf{s} = \int_{V} (\mathbf{S}_{\alpha} - \frac{\alpha}{\rho} \frac{D\rho}{Dt}) dV - \int_{V} \frac{1}{\rho} \nabla \cdot (\alpha \rho \mathbf{v}_{d}) dV$$
 (4)

where \mathbf{v}_d is the diffusion velocity of the aqueous phase, and \mathbf{S}_a is the user-defined source term of the water phase.

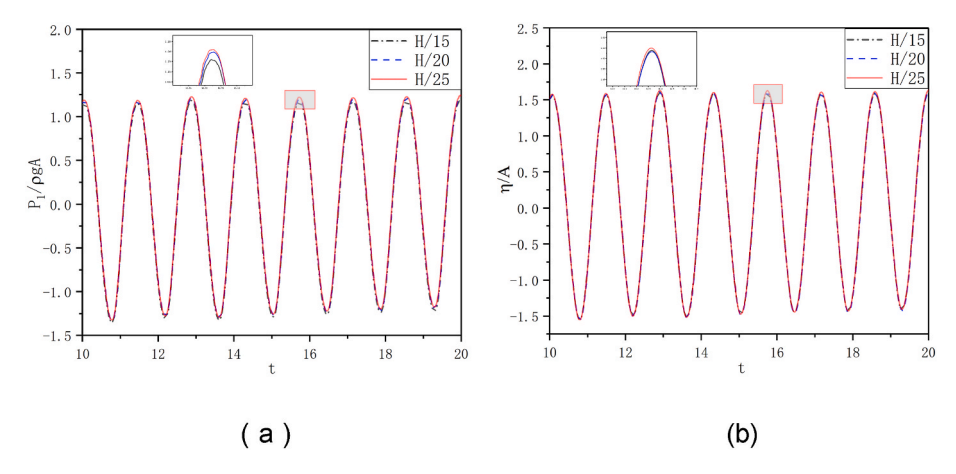


Fig. 7. Comparison of simulation results with different mesh sizes: (a) Pressure values at point S_1 ; (b) wave elevation values at point G.

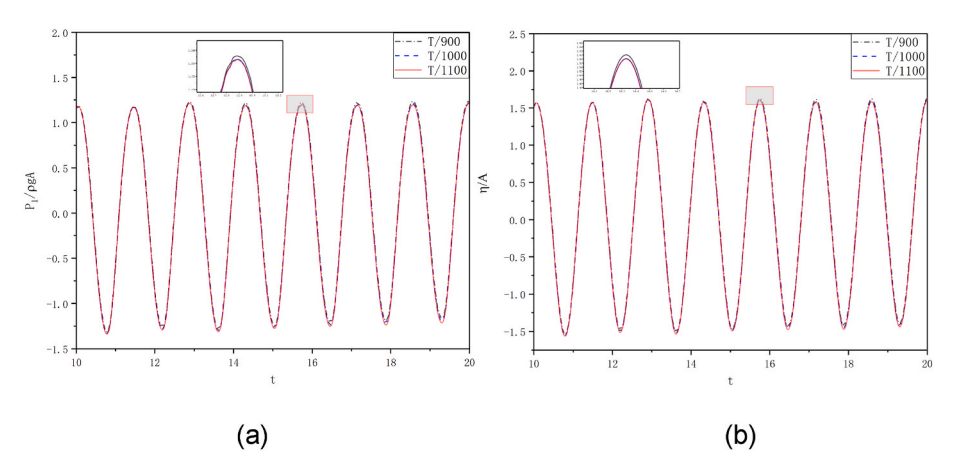


Fig. 8. Comparison of simulation results with different time steps: (a) Pressure values at point S_1 ; (b) wave elevation values at point G_1 .

Table 3The wave parameters for verifying the numerical model.

	H (mm)	h (m)	L (m)	kh
Examined case	512	1	3.16	1.99

3.3. Numerical wave generation and absorption

The first–order Stokes wave is used to represent the linear regular wave in this simulation with wave surface equation $\eta=A\cos(\omega t-kx)$, where A is the amplitude of the wave and ω is the wave

frequency. To simulate wave absorption in the wave tank, a wave resistance is set at the end of the numerical water tank. It is realized by

adding the resistance term to the velocity equation.

The resistance term S_z^d is as below:

$$S_z^d = \rho(f_1 + f_2|w|) \frac{e^k - 1}{e^1 - 1}$$
 with
$$k = (\frac{x - x_{sd}}{x_{ed} - x_{sd}}) n_d$$
 (5)

where w is the vertical velocity component, f_1 , f_2 , and n_d are damping parameters, x_{sd} is the wave damping starting point, which propagates in the x-direction and x_{ed} is the wave damping end point (inlet and outlet boundary).

The acting length of the damping region is twice of the wavelength (λ) , which can be set to obtain the best effect of wave elimination [32].

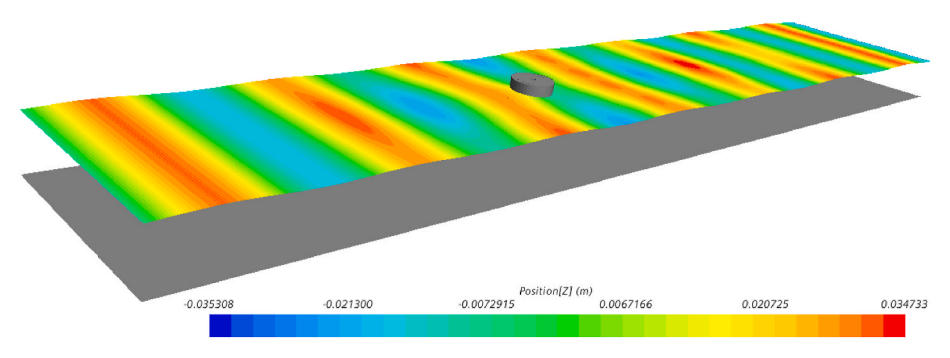
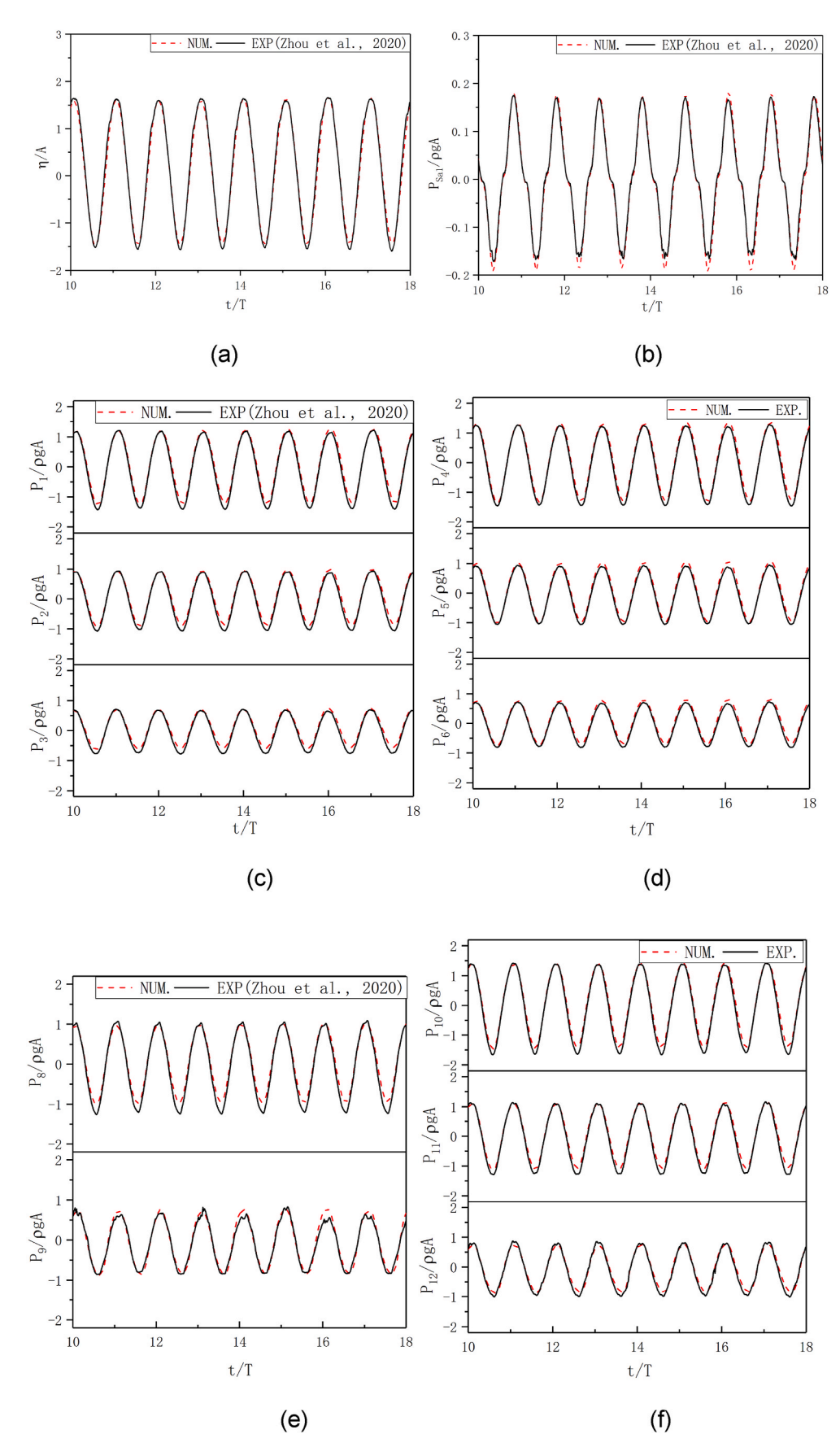


Fig. 9. Water surface elevation during wave propagation.



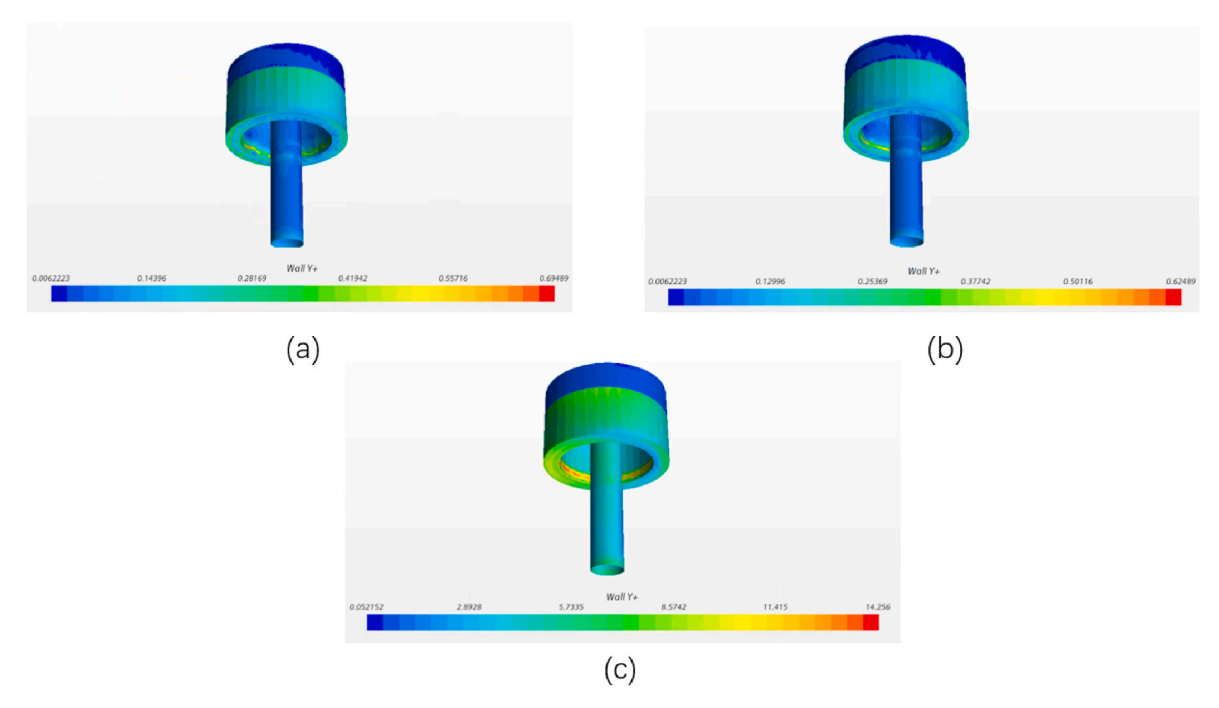


Fig. 11. y + value distribution at t = 39.7s for: (a) SST $k - \omega$; (b) Standard $k - \omega$; (c) Realizable $k - \varepsilon$.

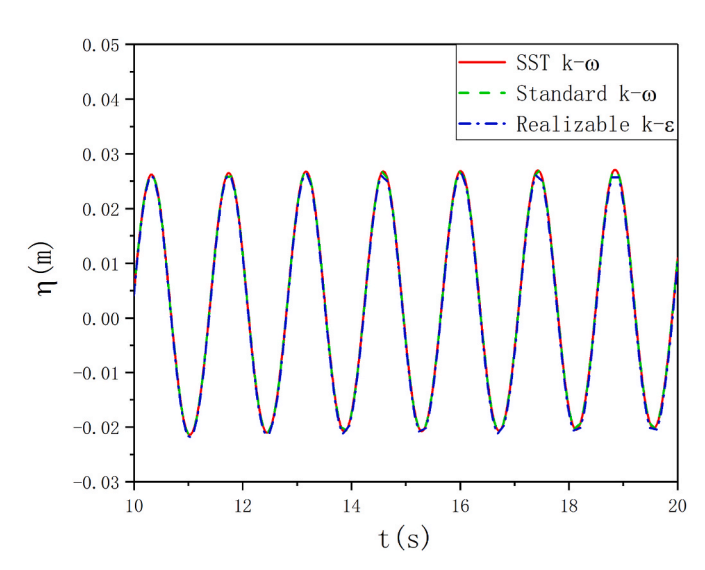


Fig. 12. Surface elevation at the wavemaker of the numerical wave tank (kh = 1.99).

3.4. Boundary conditions

Fig. 4 shows the definition of various boundaries related to the examined physical problem. For the boundary conditions of the numerical water tank, the upper side is defined as the pressure outlet boundary, where the backflow turbulence intensity is set equal to 5% and the outlet boundary backflow turbulence viscosity ratio equals to 10. The bottom is defined as the nonslip boundary, and the two tank sides are defined as slip wall. The entrance of the numerical water tank is defined as the velocity entrance boundary condition, and the entrance boundary is directly designated as the velocity of the first-order Stokes wave. The numerical calculation uses a two-phase flow model. By adding water and air phases, the VOF is used to track the free surface. For the interpolation of the physical quantity and its derivative on the control volume interface, the second-order upwind style is used for calculation.

3.5. Turbulence models

In this paper three different turbulence models will be used, nasmely, the standard $k-\omega$ model, the SST $k-\omega$ model and the realizable $k-\varepsilon$ model. The standard $k-\omega$ model is based on the Wilcox $k-\omega$ model [33], which was modified to take into account low Reynolds number, compressibility and shear-flow propagation. The SST $k-\omega$ turbulence model was developed by Menter [34]. The realizable $k-\varepsilon$ turbulence model is named because it satisfies the achievable condition. The theoretical idea was first proposed by Shih et al. [35] The transport equations of all models are shown in Table 2.where x_i is the position vector, u_i is the velocity vector, μ is the molecular viscosity, τ_{ij} is the Reynolds stress tensor, G_k is related to the turbulent mixing energy k caused by the average velocity gradient, G_b is the value due to buoyancy in the turbulent mixing energy k and Y_M represents the contribution of pulsation expansion to compressible turbulence.

The standard $k-\omega$ turbulence model is mainly based on the solution of the two equations of turbulence kinetic energy (k) and specific dissipation rate (ω) , the SST $k-\omega$ turbulence model retains the accurate solution of the $k-\omega$ model near the wall region and simultaneously realizes the independence of the $k-\varepsilon$ model in the outer part of the boundary layer. Compared with the other two models, the realizable $k-\varepsilon$ model adopts a new turbulent viscosity formula whose value is related to the mean strain rate.

3.6. Hydrodynamic efficiency of OWC

In OWC devices, the capture width is used to define their hydrodynamic efficiency. Generally, the formula of hydrodynamic efficiency can be determined as [10].

$$\xi = \frac{P_{owc}}{P_{inc}D} \tag{6}$$

where D is the characteristic length of the OWC device, P_{inc} is the time average energy flux of the incident wave and P_{owc} is the average power captured by the OWC device. P_{inc} and P_{owc} can be expressed by the following formula:

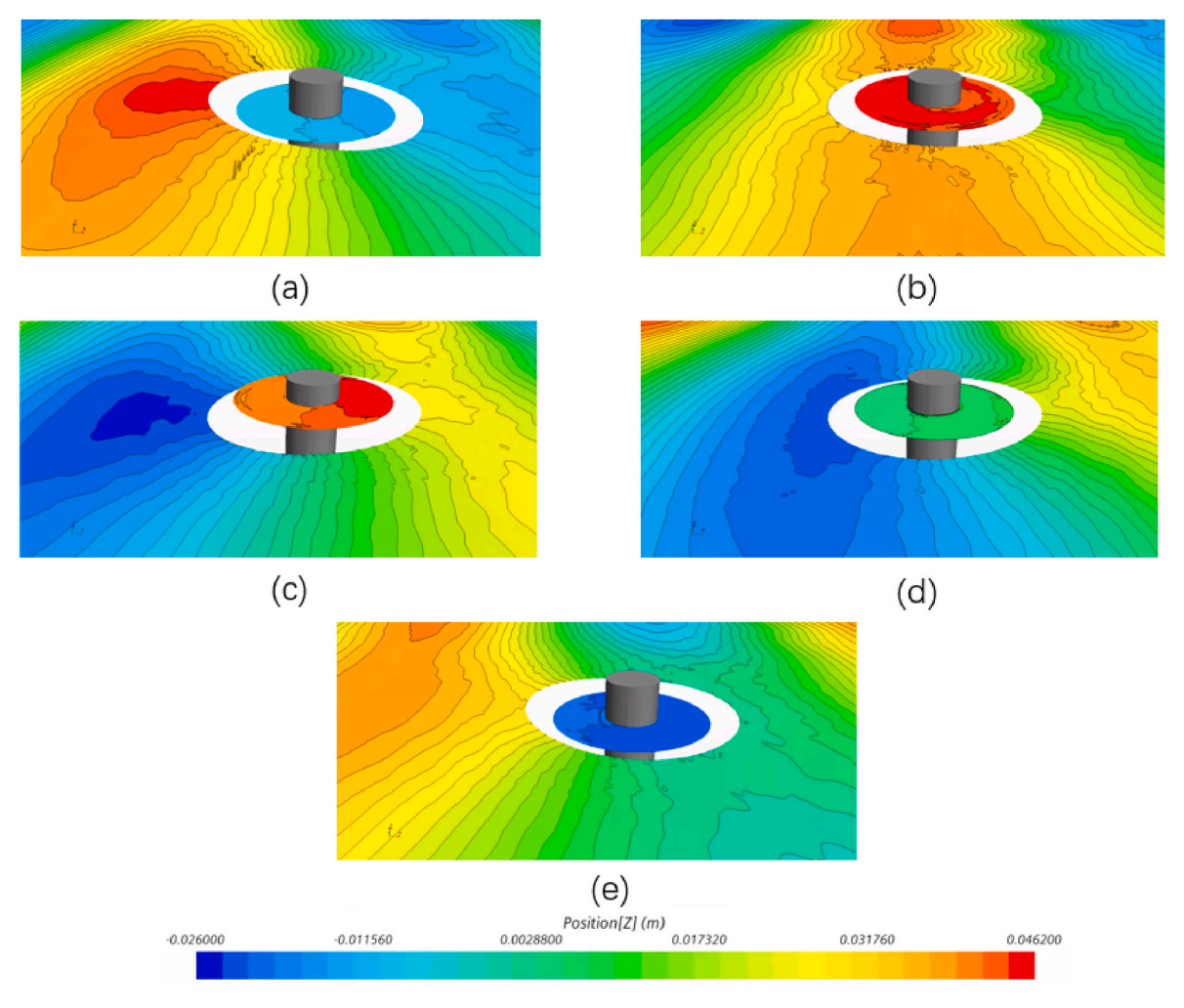


Fig. 13. Wave elevations near the OWC system simulated using the SST $k-\omega$ turbulence model at different times: (a) time = T/5; (b) time = 2T/5; (c) time = 3T/5; (d) time = 4T/5; (e) time = T.

$$P_{owc} = \frac{1}{T} \int_0^T \Delta P_{air} q(t) dt \tag{7}$$

where T is the period of the incident wave, ΔP_{air} represents the air pressure in the chamber, q(t) is the instantaneous volume flow driven by the water column, which is determined by $q(t) = A_w \frac{\partial \eta}{\partial t}, A_w$ is the cross sectional area in the chamber and η is the elevation of the water surface in the chamber.

The time average energy flux of the incident wave P_{inc} is

$$P_{inc} = \frac{\rho g A^2 \omega}{4k} \left(1 + \frac{2kh}{\sinh 2 kh} \right) \tag{8}$$

where A and ω can be determined by the wave dispersion equation: $\omega^2 = gk \tanh(kh)$.

4. CFD simulation

The software tool STAR-CCM+ is used to simulate the air-water two phase interaction problem for integrating an OWC with a fixed-breakwater.

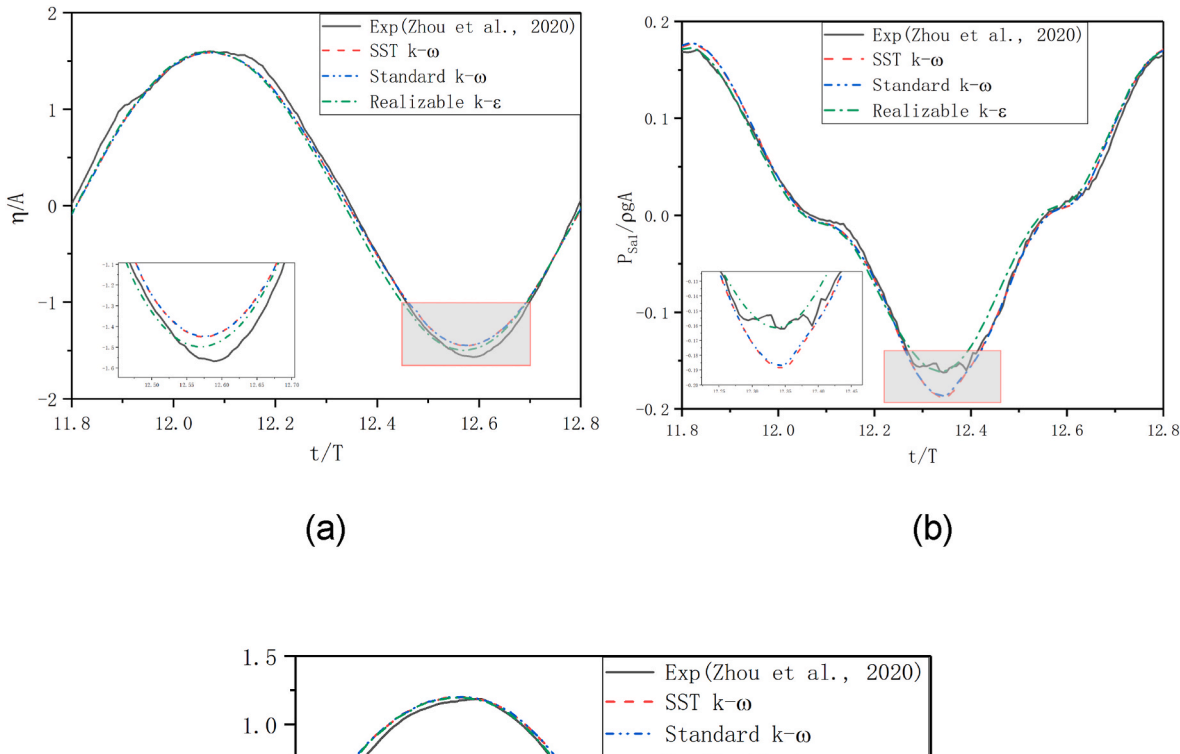
4.1. Numerical implementation

Based on the experiment, the numerical wave tank model (Fig. 3) is established. STAR-CCM + software uses a predictor-corrector method to link the continuity and momentum equations. The CFD model

implemented in the present study assumes incompressible flow in the OWC chamber. The simulation uses the segregated flow and uses the VOF method to capture the free surface. All waves in the numerical simulation are first-order Stokes waves. By setting the velocity of the water at the entrance, the waves propagating in the experimental flume can be simulated. The top of the numerical water tank was set as the pressure outlet boundary, meaning that a hydrostatic wave pressure is defined at the top boundaries. The investigation of Elhanafi et al. [36] showed that when hydrostatic pressure or constant atmospheric pressure is used at the top boundary, the definition of these two boundary conditions will not affect the simulation results. The Euler overlay method (EOM) [37] is used to address the wave reflection at the inlet of the numerical tank. Because of the difference between the analytical wave information generated in the specified region and the actual wave information, it is necessary to transform the theoretical solution of the discrete Navier-Stokes equation into a simplified numerical solution. The corresponding source term is added to the governing equation to eliminate the problem of surface wave reflection. The source term is given by

$$S(\varphi) = -c(\varphi - \varphi^*)$$
 with $c = c_0 \cos^2(\pi x/2)$ (9)

where $S(\varphi)$ is the source term corresponding to φ (the velocity distribution of instantaneous wave particles in the Z direction). To make the solution of the equation more accurate, a distance-related coefficient c is introduced into the equation. Also, c_0 is the maximum forcing coefficient



1. 0

0. 5

-1. 0

-1. 5

-1. 5

-1. 18

12. 0

12. 2

12. 4

12. 6

12. 8

t/T

(c)

Fig. 14. Comparison of turbulence models for a wave period time: (a) surface elevation at G point; (b) air pressure at S_{a1} point; (c) pressure at S_{1} point (kh = 1.99).

and x is the relative distance within the EOM region. Equation (9) can be obtained, and the closer the distance to the wave inlet is, the greater the forced value will be.

4.2. Convergence analysis

In the CFD numerical model, the setting of the mesh size is a critical factor, and its characteristics determine the degree of numerical efficiency. Initially, a convergence analysis was carried out in the developed numerical flume. According to the velocity distribution of water particles along the direction of the water depth, water particles near the free surface are moved more violently; the mesh close to the free surface should be relatively small. With increasing water depth, the velocity of water particles decreases gradually, and the corresponding mesh size can become larger. At the same time, the mesh around the structure and

related boundaries are divided, as shown in Fig. 4. The base dimension is the size of the mesh in the Z direction in a region of wave height length at the free surface. Three basic dimensions (H/15, H/20, and H/25, where H is wave height) are selected to analyze the convergence of the mesh.

The arrangement of the measuring points of different physical quantities is shown in Fig. 6. S_1 , S_2 ... S_{12} are underwater pressure sensors. S_{a1} and S_{a2} are pressure sensors placed on the top inside of the chamber. The wave gauge G is used to measure the surface elevation at a given point. The calculated response values of the pressure sensor S_1 and wave gauge G are used to judge the accuracy of the different meshes and conclude which meshes will be selected for the purposes of the paper.

Fig. 7 shows the time series of the pressure value of S_1 (using a dimensionless value $P_1/\rho gA$) for the time range of 10 s–20 s (wave height H=512 mm, kh=1.99). It can be seen that the pressure values under the three grid sizes tend to be approximately the same. With

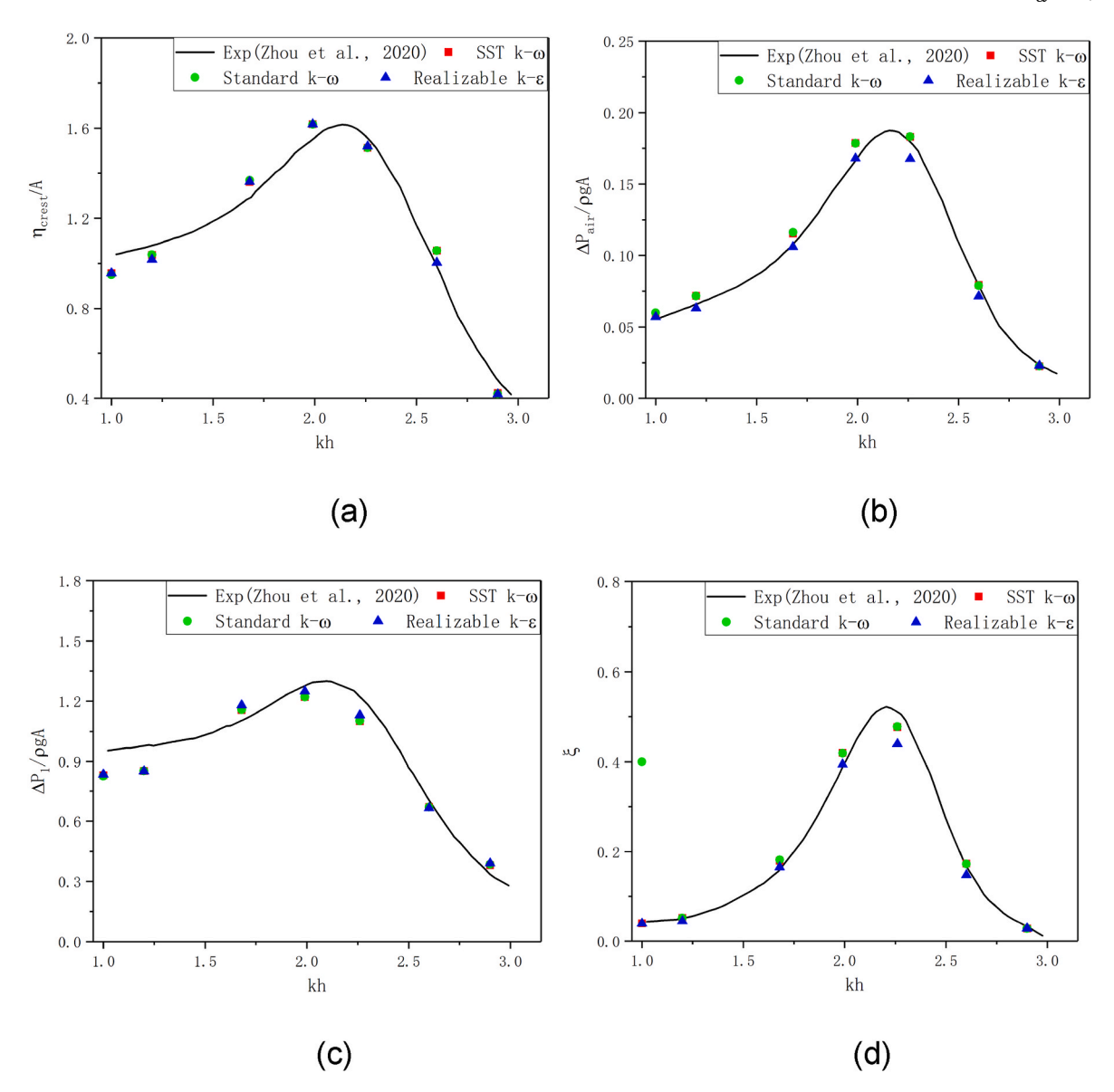


Fig. 15. Comparison of three turbulence models with experiments under different kh values for: (a) surface elevation at the G point; (b) air pressure at the S_{a1} point; (c) pressure at the S_1 point; (d) hydrodynamic efficiency.

Table 4 Errors of three turbulence models under different kh values (%).

kh								
$k - \varepsilon$ model		1	1.2	1.68	1.99	2.26	2.6	2.9
δ_n	SST	4	3.99	5.17	4.11	2.92	6.39	13.7
·	Standard	3.94	3.94	5.72	4.11	2.84	6.45	14.8
	Realizable	6.11	6.11	5.33	4.14	2.41	1.46	15.3
$\delta_{\Delta p_{air}}$	SST	4.31	8.1	6.49	6.96	1.82	0.42	4.91
	Standard	7.5	8.2	7.2	6.85	1.95	0.12	3.98
	Realizable	2.63	4.38	1.71	0.98	7.05	10.6	2.17
$\delta_{\Delta p_1}$	SST	14.46	14.5	4.46	4.62	11.12	5.2	12.1
•	Standard	15	14.6	4.74	4.51	10.93	5.26	13.2
	Realizable	13.77	14.9	6.52	2.22	8.17	5.93	14.4
δ_{ξ}	SST	7.16	1.51	10.9	7.57	7.03	3.34	12.75
	Standard	4.96	1.57	12.12	7.46	6.8	2.89	12.8
	Realizable	8.56	14.14	3.28	1.65	16.12	12.9	11.68

increasing mesh size, the values of the wave crest and wave trough tend to become similar. Based on Fig. 6, the average values of the three grid sizes have a similar trend and gradually becoming identical. The pressure peak value difference between the two denser grids and the third

grid is 4.08% and 1.65%, while, the trough value difference is 3.68% and 1.56%, respectively. Similar results are obtained from the average values of the peak and valley values of the surface elevation. From the above results, it can be concluded that H/20 is selected as the grid that is

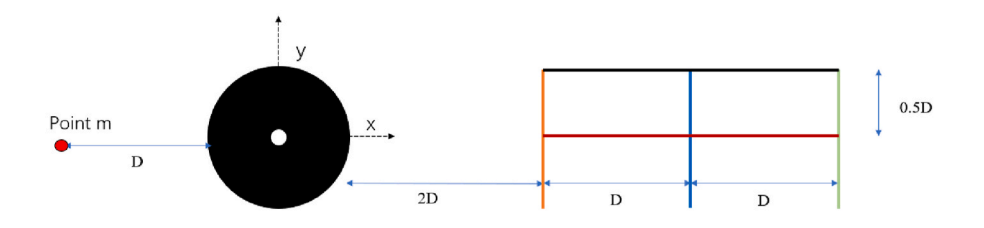
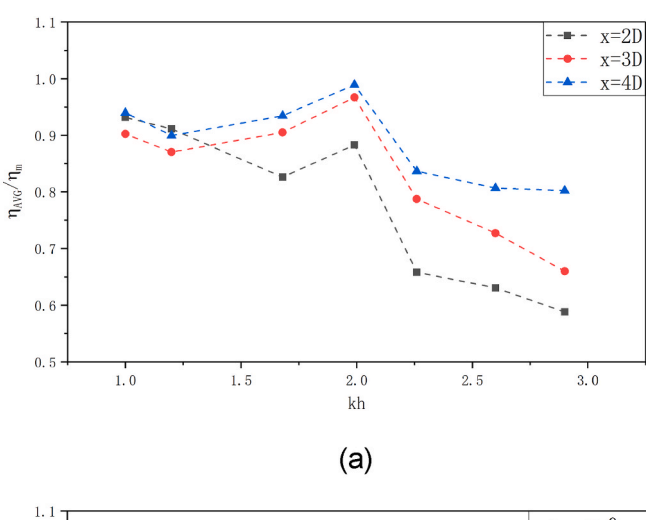


Fig. 16. The diagram of measurement points about the decrease of incident wave.



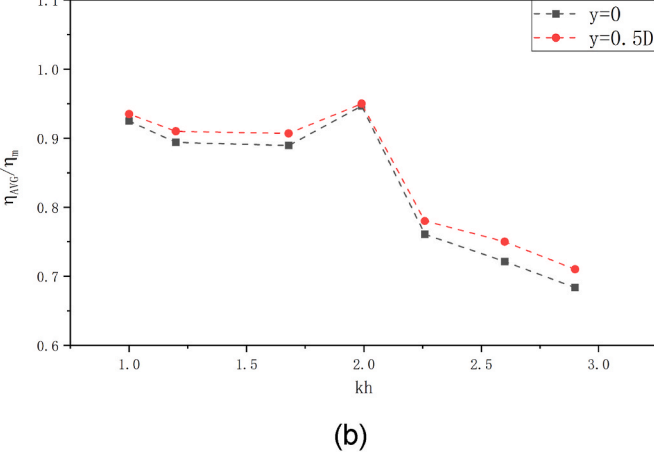


Fig. 17. Comparison of η_{AVG}/η_m values under different kh values: (a) Lines with different x values; (b) Lines with different y values.

used for the rest of the paper.

Another possible factor that causes numerical uncertainties is the choice of the time step. A comparative study for different time steps, T/900, T/1000, and T/1100, was conducted (where T is the period of the wave). In Fig. 8 this comparative study is presented; it is noted that those results correspond to the H/20 grid. The difference between the maximum time step and the minimum time step is only 2.23%. In the

rest of the paper, the time step T/1000 is used.

4.3. Numerical model verification

To verify the correctness of the developed numerical model, the calculated results are compared with relevant experimental data [29]. The parameters of wave propagation are shown in Table 3, where H is the wave height, h is the water depth and L is the wavelength. The response values that are compared correspond to the measurement points in Fig. 5 for the period between the 10th and the 18th wave cycles. The process of wave propagation is shown in Fig. 9.

Fig. 10 shows the time series at the measuring points. In general, the numerical simulation results are in very good agreement with the experimental data. Fig. 10(a) shows the time series of surface elevation inside the OWC device. It can be seen that there is a certain gap between the numerical simulation results and the experimental results at the wave trough, which is related to the numerical dissipation of the selected grid. In addition, the distribution of wave height time series with time is regular. Moreover, Fig. 10(b) shows the time series of air pressure values at point S_{a1} . In general, the numerical simulation results are consistent with the experimental results. Fig. 10(c)–(f) show the time series of the hydrodynamic pressure measured at points S_1 , S_2 ... S_{12} . It is clear that numerical dissipation still has impact on the numerical simulation results at the trough of the regular waves. It is worth noting that the pressure at the measuring point S_7 was removed since the sensor was damaged in the experiment.

5. Results and discussions

5.1. Wave conditions

Before starting the simulation of the different turbulence models, the y+values for the three turbulence models are estimated. The sensitivity analysis is carried out for three turbulence models with various y+values. The wave elevation at point G, air pressure at point S_{a1} and the pressure at S_1 are compared to experimental results to find the proper y+value for each turbulence model. Finally, the y+value of the realizable $k-\varepsilon$ turbulence model is determined equal to 29, while, for the other two models the y+value equals to 4. Fig. 11 shows the distribution of y+values at specific time instances.

To explore the effects of using different turbulence models in the numerical simulation of the OWC device, the kh numbers are selected to be 2.9, 2.6, 2.26, 1.99, 1.68, 1.2 and 1, and the water depth of all examined conditions is 1 m. The wave is provided as input from the velocity entrance boundary to simulate the wave forward process based

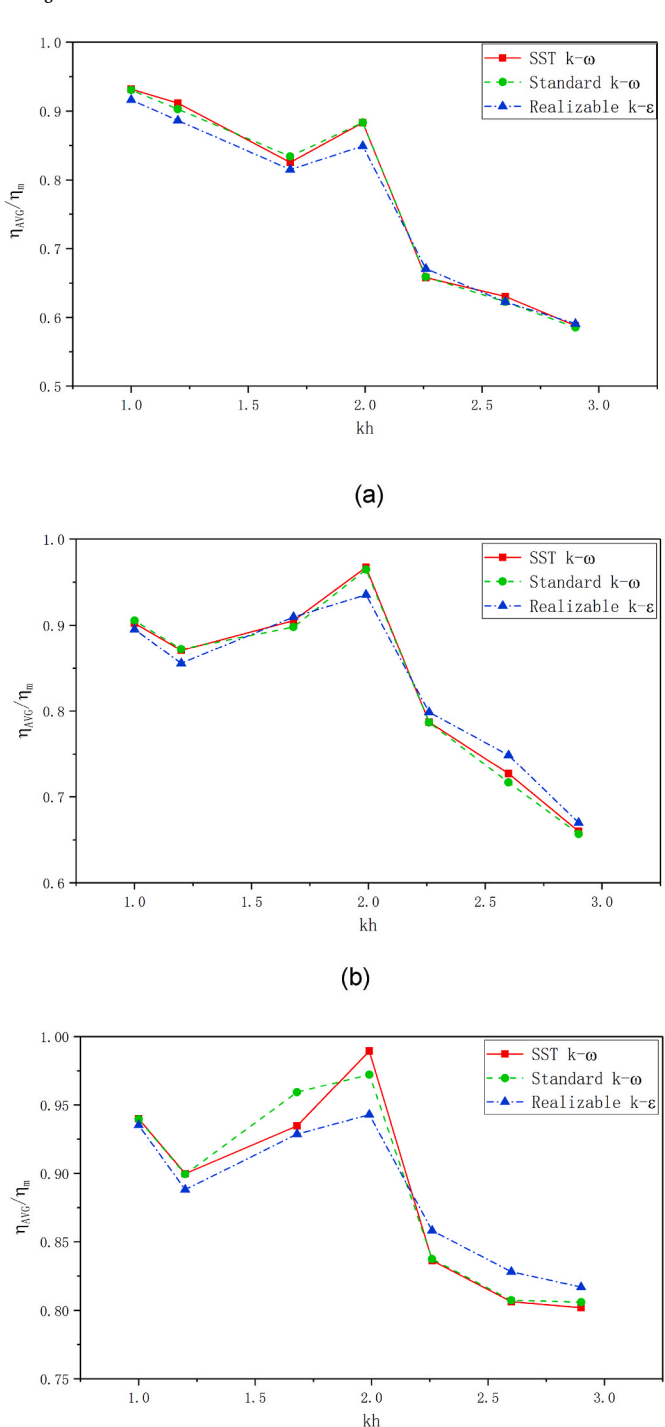


Fig. 18. Comparison of η_{AVG}/η_m values of three turbulence models: (a) line x = 2D; (b)line x = 3D; (c)line x = 4D.

(c)

on the experiment.

Fig. 12 presents the surface elevation at the wavemaker in the numerical simulation. It can be seen that when different turbulence models are selected, the incident conditions of waves are always consistent, which ensures that the difference in numerical simulation results is attributed to the different turbulence model. Fig. 13 shows the wave runup near the OWC system when the SST $k-\omega$ turbulence model is used. The wave propagates in the direction of the structure, the wave distribution in the entire chamber is almost uniform. In addition, there is a certain phase difference between the wave inside the chamber and

outside.

5.2. Differences between turbulence models

5.2.1. Comparison between numerical simulation and experiment

To accurately analyze the difference of various measuring points in the numerical simulations under different turbulence models, time series that are referring to one wave period are selected. Fig. 14 shows that the results of the models with use of the three turbulence models are generally in good agreement with the experimental results, but there are some differences mainly in the trough of wave. The error difference between experimental data and numerical prediction is defined as $\delta_N =$ $|rac{N_{exp}-N_{num}}{N_{num}}| imes 100\%$. The error δ_η for the model which uses the SST k-1 ω turbulence model for surface elevation is 5.17%, while, for the model which uses the standard $k - \omega$ turbulence model is 5.72%. The two turbulence models are very similar in solving the Navier-Stokes equation, which makes their errors basically similar. Same conclusion can be obtained from Fig. 14(b) and (c). The results obtained by the realizable $k - \varepsilon$ turbulence model are closest to the experimental values. For all three models with the same "nature" (two equation models), some differences from the experimental data are expected. Because those models lack sensitivity to unfavorable pressure gradients resulting in an overestimation of shear stress. For the case of the 'Realizable $k - \varepsilon$ ' model and by invoking the used realizability constraints, an improvement of the comparisons between experimental data and numerical prediction is observed at trough.

Fig. 15 shows the comparison of the three turbulence models with the experimental data under different kh values. In general, the three turbulence models have good results compared with the experiment. Fig. 15(a) and (b) show that the values calculated by the realizable *k* ε turbulence model under different kh conditions are smaller than those calculated by the other two models. As the value of kh increases, the difference becomes more obvious. Fig. 15(c) shows the comparison of the pressure at point S_1 under different kh. The figure shows that the pressure of the three turbulence models changes insignificant with the change of kh. The hydrodynamic efficiency represents the ratio of the extracted power of the OWC device to the incident average wave energy flux. Among the three models, the results of the SST $k-\omega$ turbulence model and the standard $k - \omega$ turbulence model are similar. However, the hydrodynamic efficiency of the realizable $k - \varepsilon$ turbulence model is lower than that of the other two models, and the gap between the results and the experiment is also the largest. Its lower air pressure in the cavity is the main factor affecting its hydrodynamic efficiency. The errors of each turbulence model and the experiment are shown in Table 4.

5.2.2. Wave attenuation performance by integrating the OWC into a breakwater

In order to measure the wave attenuation effect of the OWC when operating as a breakwater, the area behind the OWC structure is divided, as shown in Fig. 16. Behind the OWC structure, five lines of different colors are defined, moreover a point m at a position of length D in front of the OWC structure is defined, as well. Thefive lines have length equal to D and extended in the shadow of the OWC structure.

The wave attenuation performance of the structure is judged by recording the maximum wave value on each straight line and the maximum wave value at point m in front of the structure. We use the physical quantity η_{AVG}/η_m to represent the performance of this structure, where η_{AVG} is the average maximum surface elevation for all lines (taking a point every 0.1D on each line) and η_m is the maximum surface elevation at point m. It can be seen from Fig. 17(a) that the value on the line where x=2D is the smallest, as expected. The farther away from the structure, the larger the η_{AVG}/η_m value becomes. This means that there is an area behind the structure where the surface elevation becomes smaller. Fig. 17(b) shows the comparison of η_{AVG}/η_m values for the two

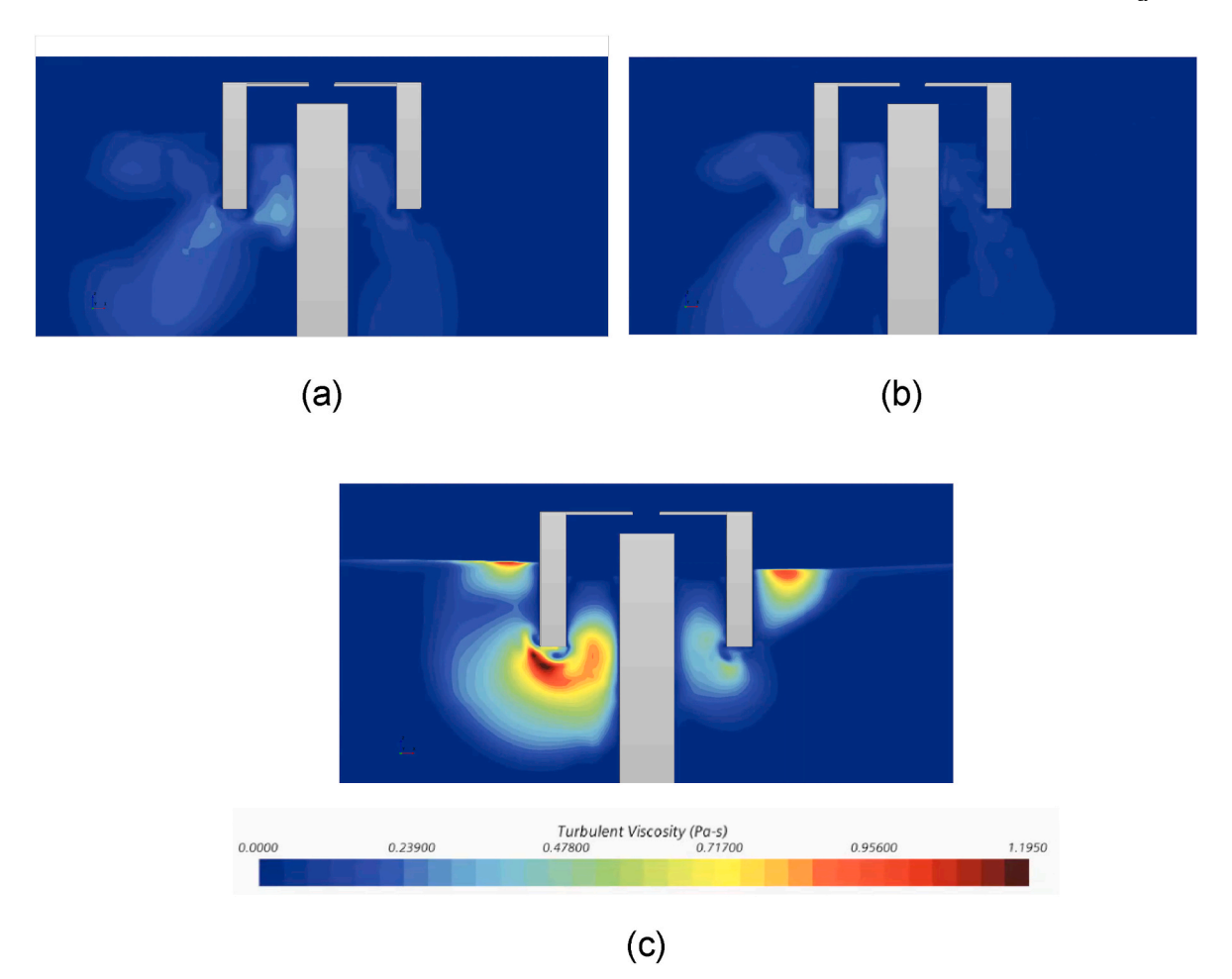


Fig. 19. Distribution diagram of turbulent viscosity in the x-o-z section ($kh = 1.99 \ t = 39.2s$): (a) SST $k - \omega$; (b) standard $k - \omega$; (c) realizable $k - \varepsilon$.

straight lines with different y values (y = 0 and y = 0.5D). As can be seen from the figure, the line with the larger y value is less affected by the OWC structure, and its η_{AVG}/η_m value is relatively large. Fig. 18 shows the η_{AVG}/η_m values for different x values for the three turbulence models. It can be seen from the figure that the η_{AVG}/η_m values of the two $k-\omega$ models are relatively close, while the value of the η_{AVG}/η_m for the realizable $k-\varepsilon$ turbulence model is slightly different from the other two models. Based on those findings it is clear that this type of OWC structure can be used as a breakwater too.

5.2.3. Comparison of pressure and velocity distribution on the cross section In Fig. 19, a turbulent viscosity contour in a x-o-z cross section is presented. It can be that the realizable $k-\varepsilon$ turbulence model has a larger turbulent viscosity in the area where the water flow velocity is high, which is related to the turbulence viscosity formula of the realizable $k-\varepsilon$ turbulence model. At the same position, the turbulence models of SST $k-\omega$ and standard $k-\omega$ results to smaller values.

Fig. 20 shows the velocity distribution of the water phase in the x-o-z section. Under the impact of waves on the OWC shell, the velocity distributions of the three turbulence models tend to be consistent. Due to the influence of the viscosity of turbulence, the velocity of the realizable $k-\varepsilon$ turbulence model around the OWC boundaries is smaller than those of the other two models.

To further study the difference between the three turbulence models at the bottom of the OWC boundaries, Fig. 21 presents the velocity and pressure along the bottom (from point A to point B). It can be seen from the figure that the realizable $k-\varepsilon$ turbulence model gives a smaller value when calculating the velocity of flow around the OWC boundaries (Fig. 22 also shows the distribution of the maximum velocity at the

bottom of the OWC for different turbulence models, and the velocity of the realizable $k-\varepsilon$ turbulence model is the smallest among the three). In the comparison of pressure values, the three turbulence models have a good consistency. This shows that there is no significant difference between the three turbulence model results when considering the pressure effect on the structure boundaries.

5.2.4. Structural wave force comparison

In addition to previous sections of considering the velocity and pressure on the OWC boundaries, the maximum force on the OWC shell and the supporting structure under the three turbulence models was also examined. When the pressure on the structure is almost the same, the speed of the water mass becomes the main factor affecting the resulting forces on the structure. Figs. 23 and 24 present the wave forces and show that the model with use of the realizable $k-\varepsilon$ turbulence model results to the lowest wave force, which is related to its lowest water mass velocity. However, in general, there is small difference in the findings among the three models.

5.2.5. Comparison of wave surface elevation distribution close to OWC system

The wave surface elevation distribution close to the OWC system is shown in Fig. 25 for the three turbulence models and kh=1.99. When the wave propagates into the OWC chamber, a significantly enlarged wave surface elevation is generated. Moreover, the wave elevation distribution in the entire chamber is almost uniform, and the fluid in the cavity has a form of motion similar to a rigid body. The same phenomenon is also observed in the [38]. The wave surface of the realizable $k-\varepsilon$ turbulence model is the lowest between the three

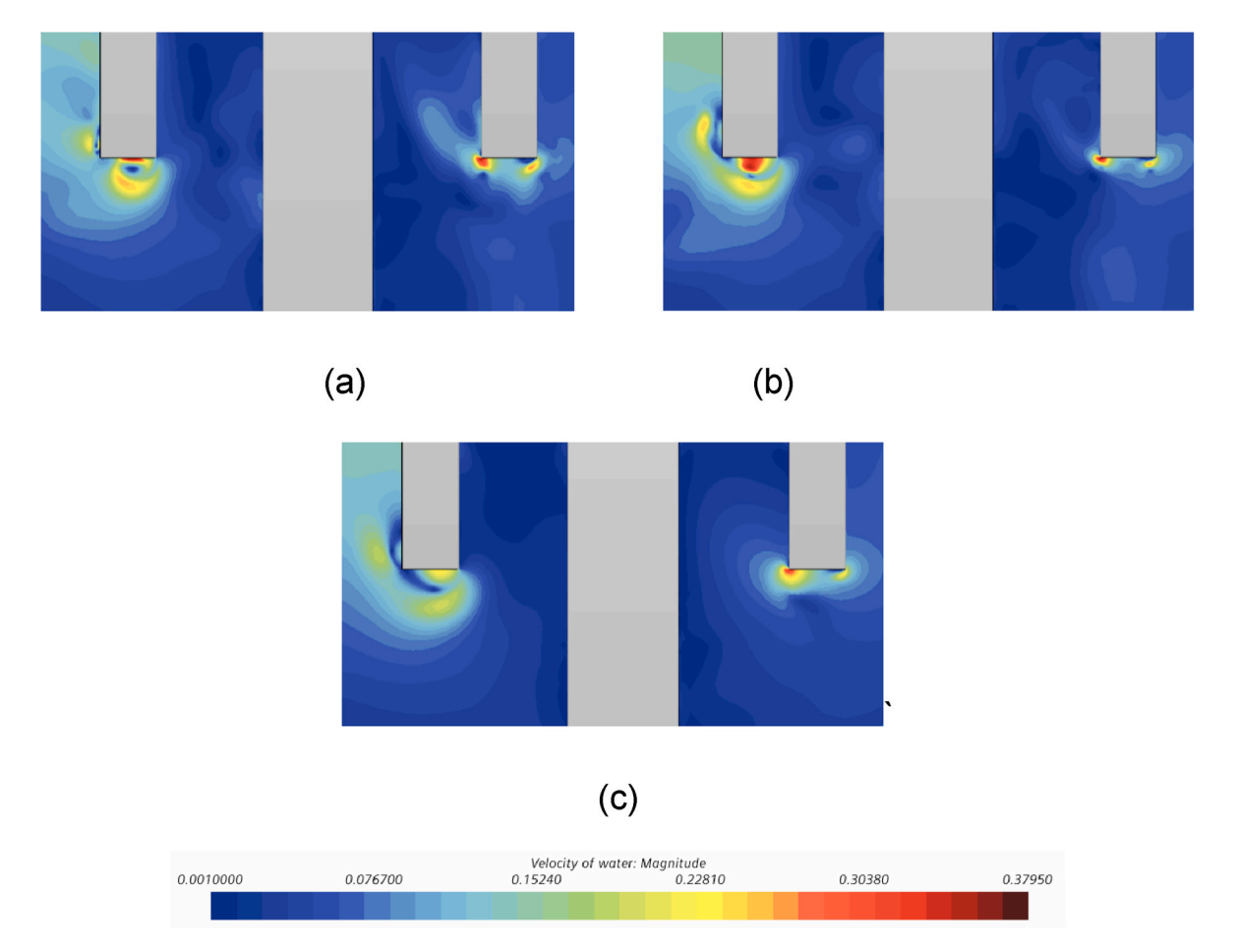


Fig. 20. The velocity distribution diagram of the water phase in the x-o-z section ($kh=1.99\ t=39.2s$):(a) SST $k-\omega$; (b) Standard $k-\omega$; (c) Realizable $k-\varepsilon$.

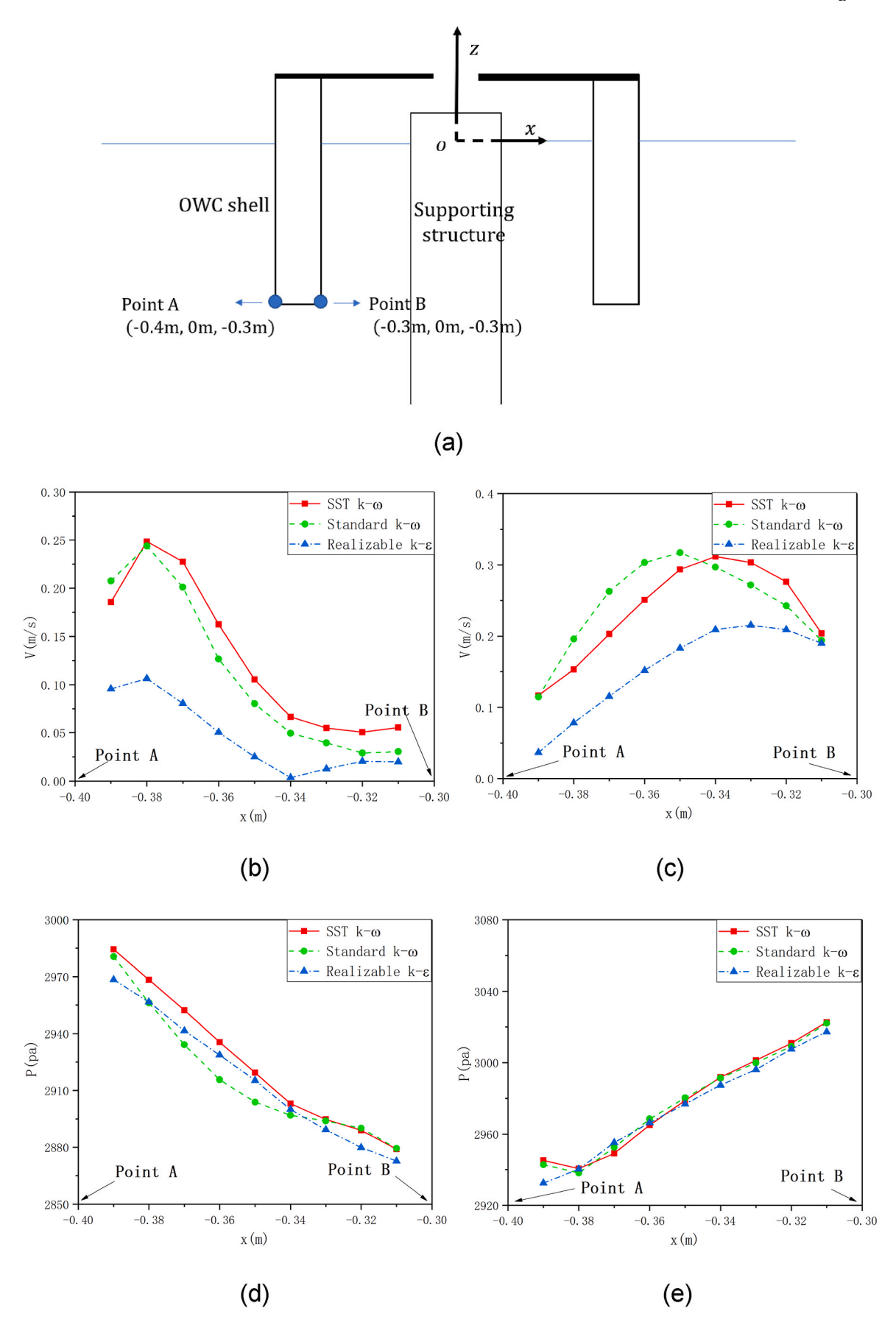


Fig. 21. Velocity and pressure distribution at the bottom of the OWC shell (kh = 1.99): (a) front view of measuring points; (b) velocity distribution at the wave peak; (c) velocity distribution at the wave trough; (d) pressure distribution at the wave peak; (e) pressure distribution at the wave trough.

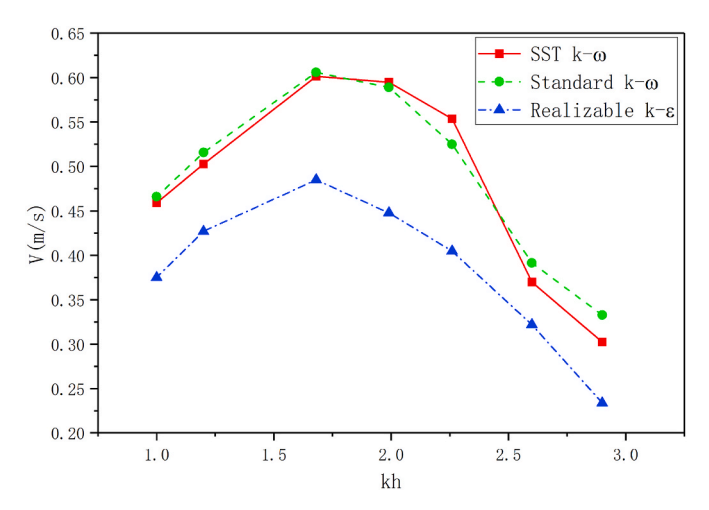


Fig. 22. Maximum velocities at the bottom of OWC for different turbulence models.

models. In order to further explore the wave surface changes of different turbulence models in the OWC chamber, Fig. 26 shows the comparison of the crest and trough values of the three turbulence models under different kh values. It can be seen from the figure that the results obtained by the three turbulence models are roughly similar, but the value of the realizable $k-\varepsilon$ turbulence model is slightly smaller than the other two models at the crests and troughs, and it can be concluded that the wave surface in the OWC chamber is the lowest among them.

5.2.6. Comparison of pressure at a specific point

The pressure in different locations is also presented in Fig. 27. Since the wave surface obtained by the realizable $k-\varepsilon$ turbulence model is lower, the pressure value is smaller compared to the other two models, but the maximum difference is only 4%. In addition, the results obtained by the SST $k-\omega$ turbulence model and the standard $k-\omega$ turbulence model are basically the same. Fig. 28 shows the comparison of the average maximum pressure at each point of the structure under different kh values. It can be seen that for different turbulence models, the maximum pressure values are almost the same. When the three turbulence models are used to perform numerical simulations of the

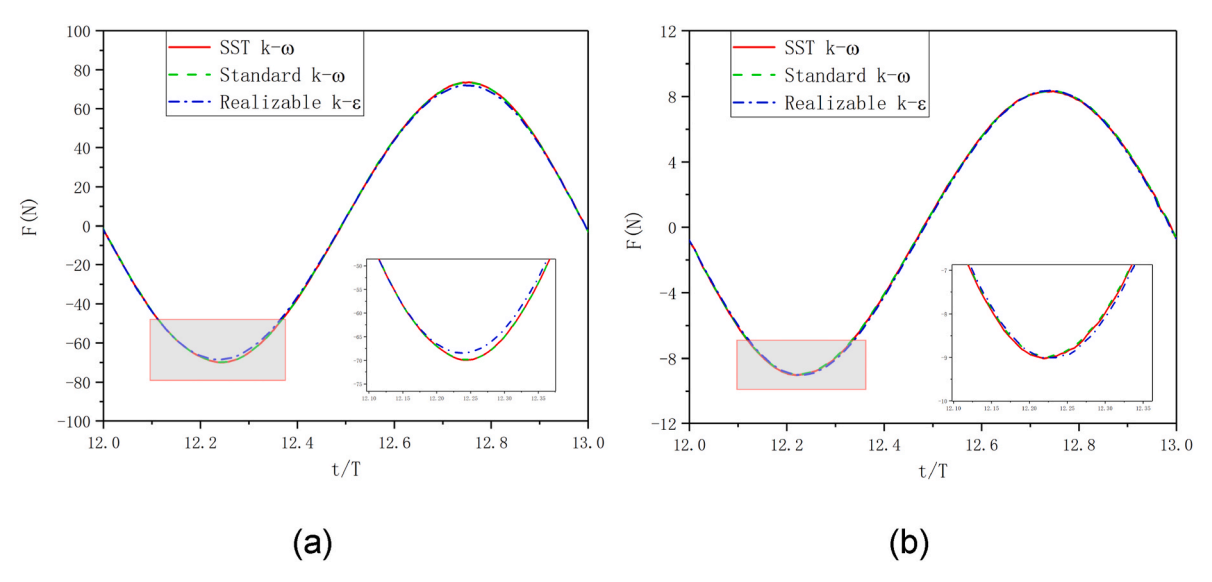


Fig. 23. Comparison of wave forces of different turbulence models in a period(kh = 1.99): (a) OWC shell; (b) supporting structure.

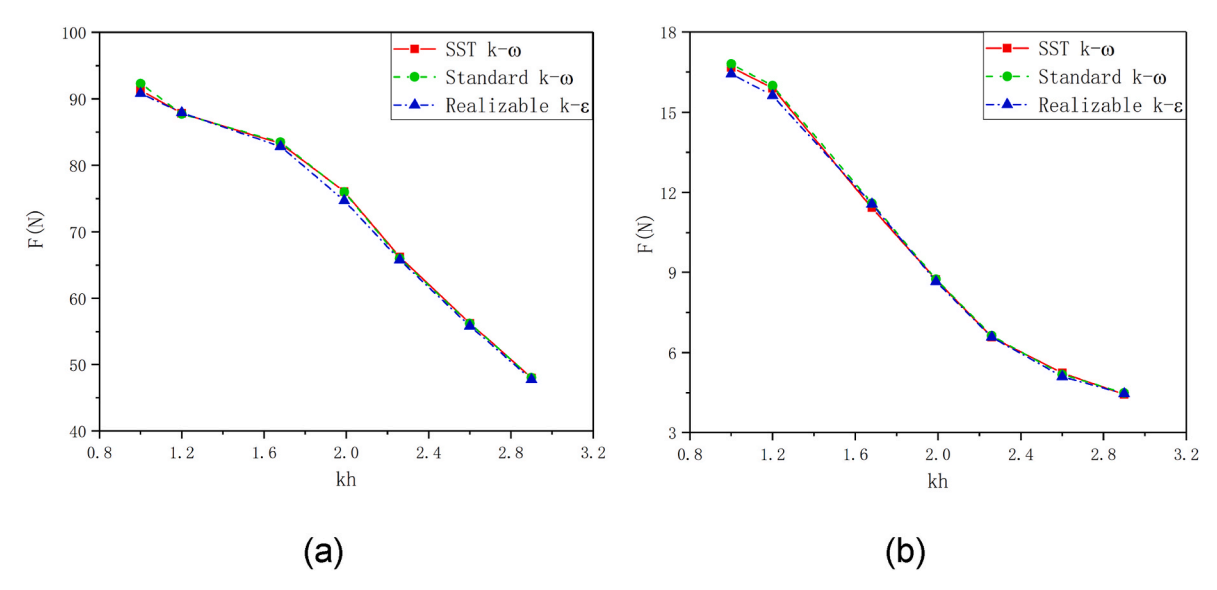


Fig. 24. Comparison of the maximum wave force experienced by different turbulence models: (a) OWC shell; (b) supporting structure.

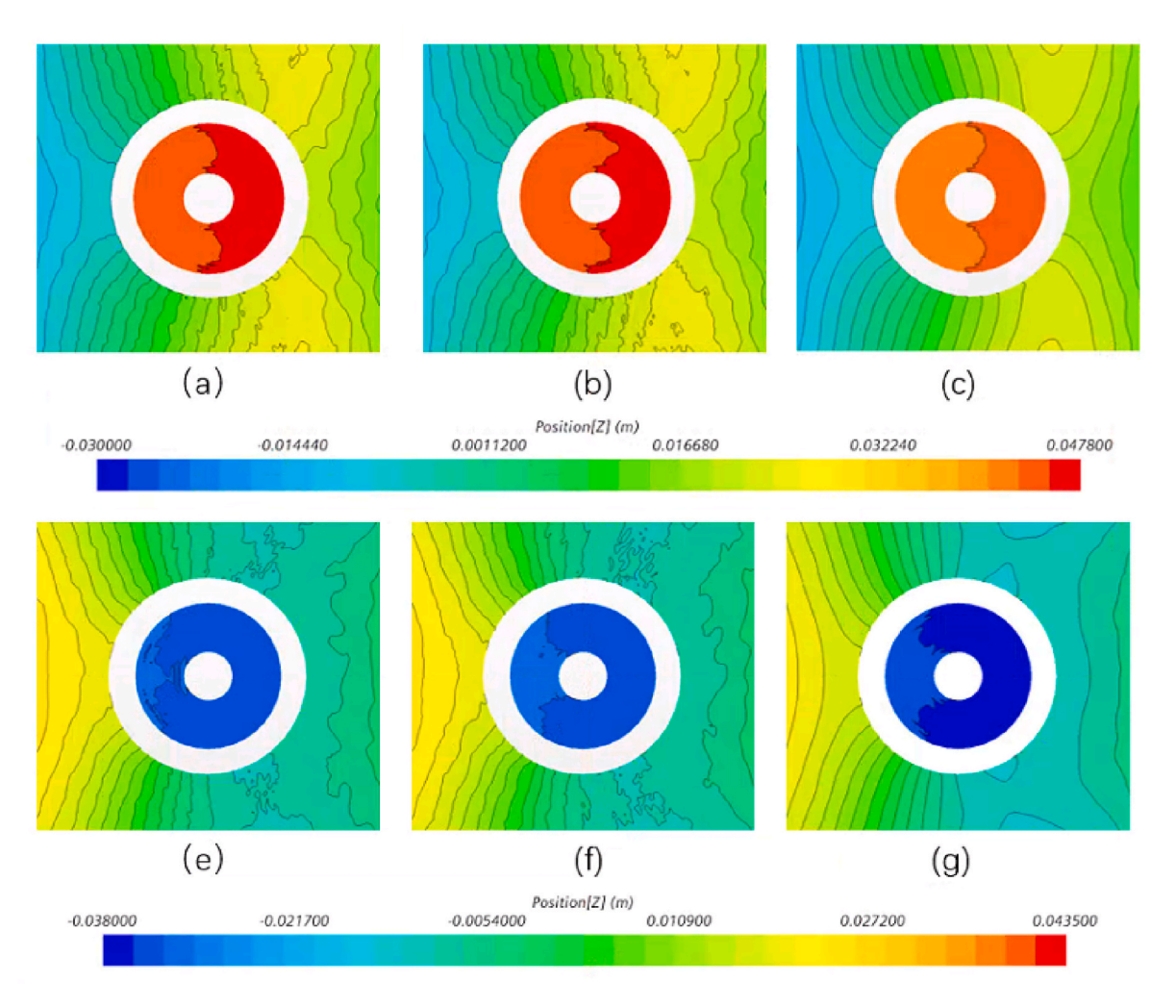


Fig. 25. Wave surface distribution diagrams of three turbulence models near the OWC system ($k = 1.99 \ t = 39.2s$) Wave crests: (a) SST $k - \omega$; (b) standard $k - \omega$; (c) Realizable $k - \varepsilon$. Wave troughs: (e) SST $k - \omega$; (f) Standard $k - \omega$; (g) Realizable $k - \varepsilon$.

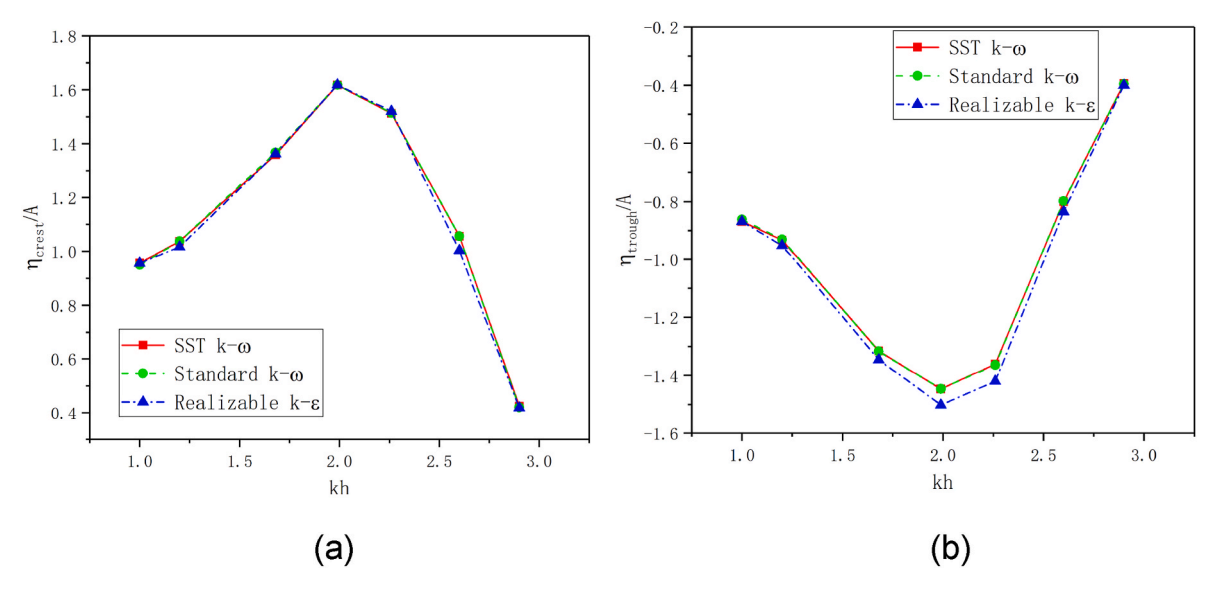
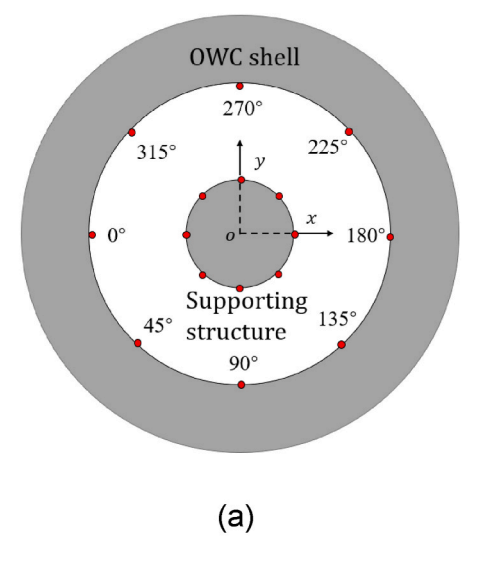


Fig. 26. Comparison of three turbulence models on wave elevation with different kh values: (a) crest values; (b) trough values.



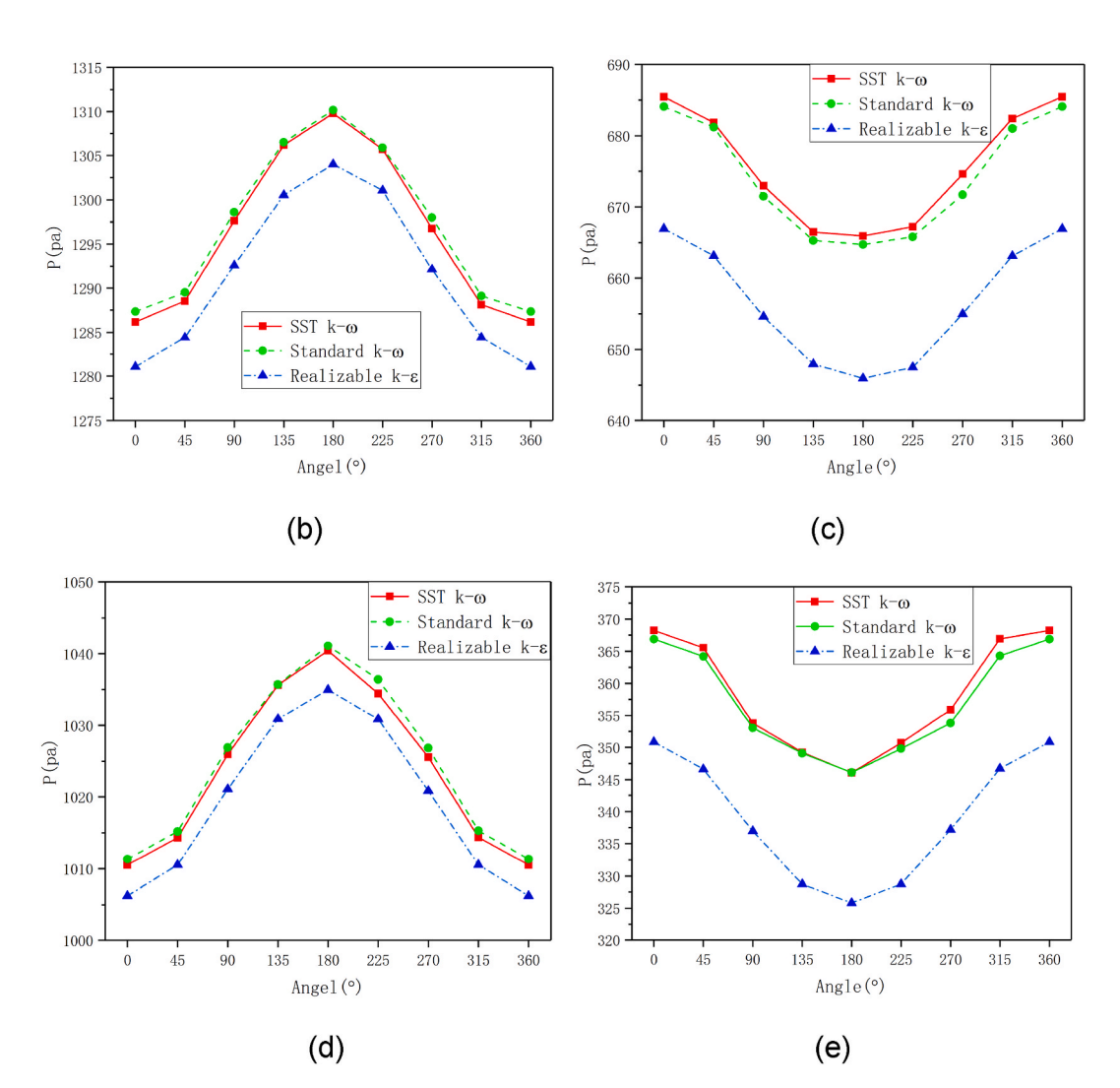


Fig. 27. Comparison of pressure values of three turbulence models ($kh = 1.99 \ t = 39.2s$): (a) top view of measuring points; (b) pressure around the supporting structure at the wave crest; (c) pressure around the supporting structure at the wave trough ($z = -0.1 \ m$); (d) pressure around the OWC shell at the wave crest; (e) pressure around the OWC shell at the wave trough ($z = -0.07 \ m$).

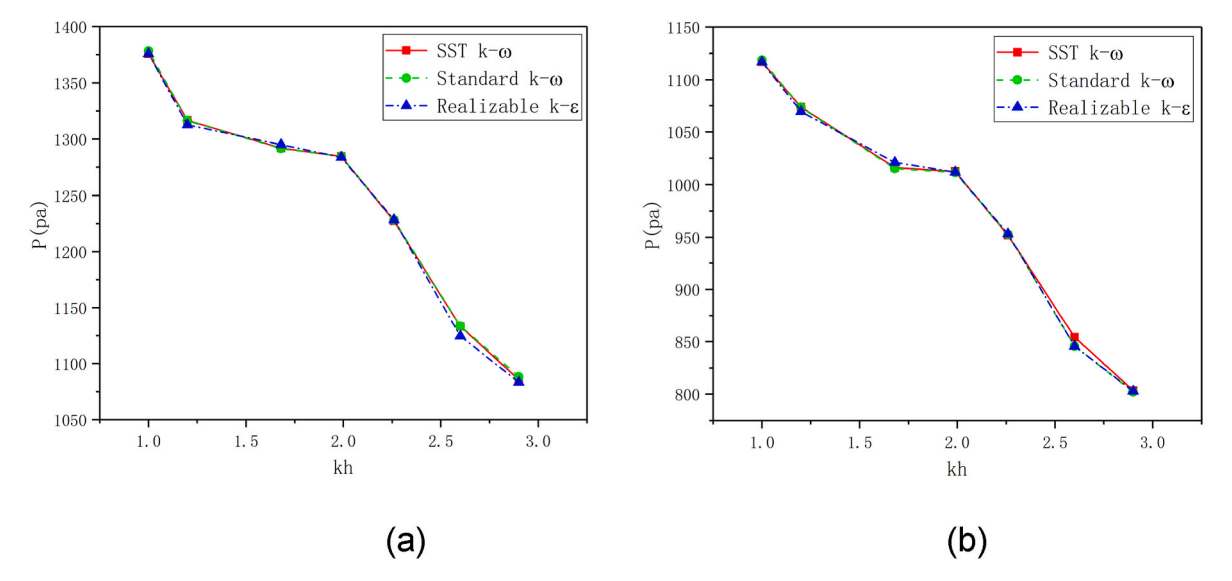


Fig. 28. Comparison of the average maximum pressure at each point of the structure under different kh values: (a) pressure around the supporting structure (z = -0.1 m); (b) pressure around the OWC shell (z = -0.07 m).

OWC device, the differences in the pressure and force of the structure are small.

6. Conclusion

In this paper, a three-dimensional CFD model of an OWC wave energy converter integrated into a fixed-breakwater is developed. After analyzing the convergence of the mesh size and time step, the hydrodynamic performance of the OWC device is studied and the numerical results are in good agreement with the experimental data. This paper also compares the simulation results of three different turbulence models and examines their efficiency for predicting hydrodynamic response quantities. The main findings of the paper are as follows:

- (1) This OWC structure has a certain positive effect of attenuating waves and it is clear that this type of structure can be used for both production of energy and wave attenuation.
- (2) The SST $k-\omega$ turbulence model has higher accuracy and is recommended for use in relevant numerical analysis simulations.
- (3) The realizable $k-\varepsilon$ turbulence model has larger turbulence viscosity than the other two turbulence models, and it mainly affects the velocity of the water point when the wave flows around the structure.
- (4) When the three turbulence models are used to perform numerical simulations of the OWC device, the differences in the pressure and force of the structure are small. However, the wave elevation and the air pressure in the OWC simulated with use of the realizable $k-\varepsilon$ turbulence model are smaller, which will make the hydrodynamic efficiency lower than that of the other two models (the maximum gap is 10%).

Author statement

This work doesn't involve the use of animal or human subjects.

Declaration of competing interest

The authors declare that they have no known competing financial interests or personal relationships that could have appeared to influence the work reported in this paper.

Data availability

The data that has been used is confidential.

Acknowledgement

This research was funded by the National Natural Science Foundation of China (Grant No. 52071058, 51939002). This work is also partially supported by LiaoNing Revitalization Talents Program (XLYC1807208), special funds for promoting high quality development from department of natural resources of Guangdong province (GDNRC [2020]016) and the Fundamental Research Funds for the Central University (DUT20ZD219). The authors acknowledge the Supercomputer Center of Dalian University of Technology for providing computing resources.

References

- Pechak O, Mavrotas G, Diakoulaki D. Role and contribution of the clean development mechanism to the development of wind energy. Renew Sustain Energy Rev 2011;15:3380-7.
- [2] Mork G, Barstow S, Kabuth A, Pontes MT. Assessing the global wave energy potential. In: ASME 2010 29th international conference on ocean. Shanghai: Offshore and Arctic Engineering; 2010. p. 447–54.
- [3] Falcão AFDO. Wave energy utilization: a review of the technologies. Renew Sustain Energy Rev 2010;14:899–918.
- [4] Ren Y, Venugopal V, Shi W. Dynamic analysis of a multi-column TLP floating offshore wind turbine with tendon failure scenarios. Ocean Eng 2022;245:110472.
- [5] Wang Y, Shi W, Michailides C, Wan L, Kim H, Li X. WEC shape effect on the motion response and power performance of a combined wind-wave energy converter. Ocean Eng 2022;250:111038.
- [6] Zhang L, Shi W, Karimirad M, Michailides C, Jiang Z. Second-order hydrodynamic effects on the response of three semisubmersible floating offshore wind turbines. Ocean Eng 2020;207:107371.
- [7] Rusu L, Rusu E. Evaluation of the worldwide wave energy distribution based on ERA5 data and altimeter measurements. Energies 2021;14(2):394.
- [8] Iglesias G, Carballo R. Wave resource in El Hierro—an island towards energy selfsufficiency. Renew Energy 2011;36:689–98.
- [9] Heath TV. A review of oscillating water columns. Philos T R Soc A Sci 2012;370: 235–45.
- [10] Morris-Thomas MT, Irvin RJ, Thiagarajan KP. An investigation into the hydrodynamic efficiency of an oscillating water column. J Offshore Mech Arct 2006;129:273–8.
- [11] Zheng S, Zhu G, Simmonds D, Greaves D, Iglesias G. Wave power extraction from a tubular structure integrated oscillating water column. Renew Energy 2020;150: 342–55.
- [12] Hashem I, Abdel Hameed HS, Mohamed MH. An axial turbine in an innovative oscillating water column (OWC) device for sea-wave energy conversion. Ocean Eng 2018;164:536–62.

- [13] Ning D, Wang R, Chen L, Sun K. Experimental investigation of a land-based dualchamber OWC wave energy converter. Renew Sustain Energy Rev 2019;105: 48-60
- [14] Haghighi AT, Nikseresht AH, Hayati M. Numerical analysis of hydrodynamic performance of a dual-chamber oscillating water column. Energy 2021;221: 119892.
- [15] McCormick ME. A modified linear analysis of a wave-energy conversion buoy. Ocean Eng 1976;3:133–44.
- [16] Evans DV. The oscillating water column wave-energy device. IMA J Appl Math 1978;22:423–33.
- [17] Zhang Y, Zou Q, Greaves D. Air–water two-phase flow modelling of hydrodynamic performance of an oscillating water column device. Renew Energy 2012;41:
- [18] Xu C, Huang Z. Three-dimensional CFD simulation of a circular OWC with a nonlinear power-takeoff: model validation and a discussion on resonant sloshing inside the pneumatic chamber. Ocean Eng 2019;176:184–98.
- [19] Shalby M, Elhanafi A, Walker P, Dorrell DG. CFD modelling of a small–scale fixed multi–chamber OWC device. Appl Ocean Res 2019;88:37–47.
- [20] Dai S, Day S, Yuan Z, Wang H. Investigation on the hydrodynamic scaling effect of an OWC type wave energy device using experiment and CFD simulation. Renew Energy 2019;142:184–94.
- [21] Cui Y, Liu Z, Zhang X, Xu C. Review of CFD studies on axial-flow self-rectifying turbines for OWC wave energy conversion. Ocean Eng 2019;175:80–102.
- [22] Cambuli F, Ghisu T, Virdis I, Puddu P. Dynamic interaction between OWC system and Wells turbine: a comparison between CFD and lumped parameter model approaches. Ocean Eng 2019;191:106459.
- [23] Simonetti I, Cappietti L, Elsafti H, Oumeraci H. Evaluation of air compressibility effects on the performance of fixed OWC wave energy converters using CFD modelling, Renew Energy 2018;119:741–53.
- [24] Liu Z, Xu C, Kim K, Li M. Experimental study on the overall performance of a model OWC system under the free-spinning mode in irregular waves. Energy 2022;250: 123779

- [25] Liu Z, Xu C, Kim K. A CFD-based wave-to-wire model for the oscillating water column wave energy Convertor. Ocean Eng 2022;248:110842.
- [26] Zhao X, Zhang L, Li M, Johanning L. Experimental investigation on the hydrodynamic performance of a multi-chamber OWC-breakwater. Renew Sustain Energy Rev 2021;150:111512.
- [27] Liu S, Ong MC, Obhrai C, Gatin I, Vukčević V. Influences of free surface jump conditions and different k—0 SST turbulence models on breaking wave modelling. Ocean Eng 2020;217:107746.
- [28] Wu Y, Hsiao S. Propagation of solitary waves over double submerged barriers. Water2017. p.
- [29] Zhou Y, Ning D, Shi W, Johanning L, Liang D. Hydrodynamic investigation on an OWC wave energy converter integrated into an offshore wind turbine monopile. Coast Eng 2020;162:103731.
- [30] Hirt CW, Nichols BD. Volume of fluid (VOF) method for the dynamics of free boundaries. J Comput Phys 1981;39:201–25.
- [31] Siemens. User guide STAR-CCM+ version 14. 2019. 06.013-R8.
- [[32]] Choi J, Yoon SB. Numerical simulations using momentum source wave-maker applied to RANS equation model. Coast Eng 2009;56:1043–60.
- [33] Wilcox DC. Reassessment of the scale-determining equation for advanced turbulence models. AIAA J 1988;26:1299–310.
- [34] Menter FR. Two-equation eddy-viscosity turbulence models for engineering applications. AIAA J 1994;32:1598–605.
- [35] Shih T, Liou WW, Shabbir A, Yang Z, Zhu J. A new k-ε eddy viscosity model for high Reynolds number turbulent flows. Comput Fluids 1995;24:227–38.
- [36] Elhanafi A, Macfarlane G, Fleming A, Leong Z. Scaling and air compressibility effects on a three-dimensional offshore stationary OWC wave energy converter. Appl Energy 2017;189:1–20.
- [37] Kim J, O Sullivan J, Read A. Ringing analysis of a vertical cylinder by euler overlay method. In: ASME 2012 31st international conference on ocean. Rio de Janeiro: Offshore and Arctic Engineering; 2012. p. 855–66.
- [38] Cong P, Teng B, Bai W, Ning D, Liu Y. Wave power absorption by an oscillating water column (OWC) device of annular cross-section in a combined wind-wave energy system. Appl Ocean Res 2021;107:102499.